FACULTY OF MATHEMATICS AND PHYSICS
Charles University

BACHELOR THESIS

Barbora Adamcová
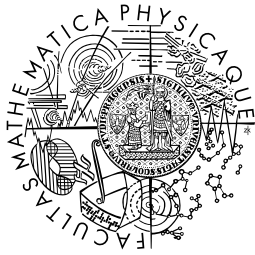
X-ray emission of star-forming dwarf galaxies

Astronomical Institute of the Charles University in Prague

Supervisor of the bachelor thesis: RNDr. Jiří Svoboda, Ph.D.

Study programme: Physics

Study branch: General Physics

Prague 2021

MATEMATICKO-FYZIKÁLNÍ FAKULTA
Univerzita Karlova

BAKALÁŘSKÁ PRÁCE

Barbora Adamcová

Rentgenové záření hvězdotvorných trpasličích galaxií

Astronomický ústav Univerzity Karlovy v Praze

Vedoucí bakalářské práce: RNDr. Jiří Svoboda, Ph.D.

Studijní program: Fyzika

Studijní obor: Obecná fyzika

I declare that I carried out this bachelor thesis independently, and only with the cited sources, literature and other professional sources. It has not been used to obtain another or the same degree.

I understand that my work relates to the rights and obligations under the Act No. 121/2000 Sb., the Copyright Act, as amended, in particular the fact that the Charles University has the right to conclude a license agreement on the use of this work as a school work pursuant to Section 60 subsection 1 of the Copyright Act.

In . . . . date . . . .

Author's signature

i

Title: X-ray emission of star-forming dwarf galaxies

Author: Barbora Adamcová

Institute: Astronomical Institute of the Charles University in Prague

Supervisor: RNDr. Jiří Svoboda, Ph.D., Astronomical Institute of the Czech Academy of Sciences

Abstract: This bachelor's thesis deals with star-forming dwarf galaxies that were proposed to host an Active Galactic Nucleus (AGN) based on the measured X-ray excess over the prediction from star-formation processes. For the studied sample, we compared different methods of X-ray luminosity calculations from the star formation rate (SFR). From the optical emission line measurements, we estimated the galaxy metallicities using three distinct methods to include the metallicity effects in the X-ray luminosity predictions. We found that the galaxy metallicities are on average sub-solar, but not sufficiently low to explain the measured X-ray luminosity. We compared the studied sample with other similar galaxies in the luminosity-SFR-metallicity plane showing their different position from purely star-forming galaxies. We discuss possible sources for the measured X-ray excess as well as the implication of the found results on the AGN diagnostics in dwarf galaxies.

Název práce: Rentgenové záření hvězdotvorných trpasličích galaxií

Autor: Barbora Adamcová

Ústav: Astronomický ústav Univerzity Karlovy v Praze

Vedoucí práce: RNDr. Jiří Svoboda, Ph.D., Astronomical Institute of the Czech Academy of Sciences

Abstrakt: Tato bakalářská práce se zabývá hvězdotvornými trpasličími galaxiemi, které byly navrženy jako hostitelé aktivního galaktického jádra (AGN) na základě naměřeného rentgenového přebytku nad predikcí z procesů tvorby hvězd. U studovaného vzorku jsme porovnali různé metody výpočtu rentgenové luminozity z rychlosti tvorby hvězd (SFR). Na základě měření optických emisních čar jsme určili metalicity galaxií pomocí tří odlišných metod tak, aby predikce rentgenové luminozity zahrnovaly účinky metalicity. Zjistili jsme, že metalicity galaxií jsou v průměru sub-solární, ale nejsou dostatečně nízké, aby vysvětlily měřenou rentgenovou luminozitu. Porovnávali jsme studovaný vzorek s jinými podobnými galaxiemi v rovině luminozita-SFR-metalicita, které ukazují jejich odlišnou polohu od čistě hvězdotvorných galaxií. Diskutujeme o možných zdrojích pro měřený přebytek rentgenového záření a také o implikaci nalezených výsledků na AGN diagnostiku v trpasličích galaxiích.

Klíčová slova: Trpasličí galaxie, tvorba hvězd, rentgenová astronomie

Contents

Preface

After the dark recombination era, the Epoch of Reionisation took place in the early Universe (for $z < 6$), during which the light from first stars and early galaxies contributed to the ionisation of the intergalactic medium and affected the observability in the universe. The responsible sources, which include star-forming galaxies and quasars, are being researched extensively.

Since the study of these high-redshifted sources would be susceptible to considerable errors, research on local galaxies with analogous properties to the early ones is conducted instead. One of the ways to probe the star formation histories of galaxies is to study their X-ray properties. The X-ray luminosity from those galaxies has been shown to be proportional to the star formation rate (SFR) (Ranalli et al., 2003; Mineo et al., 2012a) and metallicity (Douna et al., 2015; Brorby et al., 2016) and this dependence can be used to research whether a galaxy might have some other source of X-ray emission, such as an AGN, if a significant excess in X-rays is measured.

Investigation on these star-forming dwarf galaxies and their X-ray properties, could help shed light on the Epoch of Reionisation and the history of galaxies and star formation. In this thesis, we study the effects metallicity can have on the X-ray luminosity for a sample of dwarf galaxies, which were shown as possible to host an AGN by Birchall et al. (2020).

1. Introduction

1.1   Epoch of Reionisation

The beginning of the cosmic history is marked by the occurrence of the Big Bang, which is estimated to have taken place around 13.8 million years ago (Planck Collaboration et al., 2020). The early history of the universe is reviewed by e.g., Chow (2008) and references therein.

The earliest moment after the Big Bang is called the Planck epoch, during which the present physical laws and theories presumably cannot be applied. It is mostly assumed that all four fundamental forces (gravitational, electromagnetic, strong and weak) were unified in a single force and carried by one gauge boson - the hypothetical graviton.

With the expansion and cooling of the universe after the Planck epoch several phase transitions from higher to lower energies occurred, which are presumed to have been caused by spontaneous symmetry breaking (Anninos, 2001). One such phase transition marks the start of the Grand Unification epoch at s, where the gravitational force split off from the previous unified force. The three forces of the Standard Model are still merged in a single force and are being described in Grand Unified Theory (GUT).

The GUTs era ended with a second phase transition as the strong nuclear interaction separated from the electromagnetic and weak interaction, which formed the electroweak force (Anninos, 2001) and started the Electroweak epoch. This phase transition is also believed to have caused the cosmic inflation during the Inflationary epoch, which is usually placed around the beginning of the Electroweak epoch.

The start of the Quark epoch is characterised by having the four basic forces distinct from each other, while the energies remain high and therefore the matter is in the form of quark-gluon plasma (Fromerth et al., 2012). The lower temperature Hadron epoch followed and the quarks were able to form hadrons, which included mesons and baryons (protons and neutrons). At around s after the Big Bang most hadron and anti-hadrons were annihilated and the Lepton epoch started. After the lepton and anti-lepton annihilated as well the Photon epoch
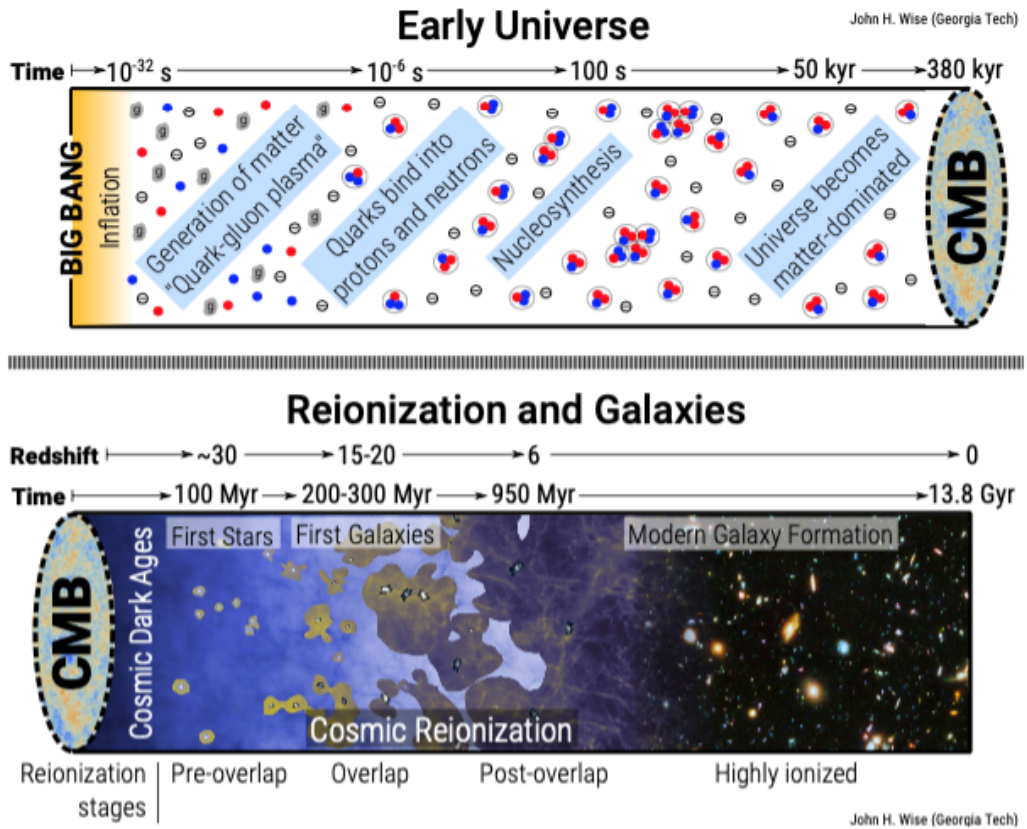
Figure 1.1: Cosmic history before (top) and after (bottom) recombination with the stages of reionisation. Figure adopted from Wise (2019).

followed, during which primordial nucleosynthesis bound protons and neutrons into elements heavier than ^{1}H. These radiation-dominated epochs are visible in the upper diagram in 1.1.

As is also apparent on 1.1 between 50 and 380 kyr after the Big Bang the universe became matter-dominated (Wise, 2019; Anninos, 2001). The universe cooled to under 3000 K and that allowed for recombination, in which the free ions and electrons recombined to neutral state (mainly neutral hydrogen and helium) (Wise, 2019; Zaroubi, 2013). Photon decoupling immediately followed and the cosmic microwave background (CMB) was created in the process.

After photon decoupling the Dark Ages epoch began about 380 kyr after the Big Bang. The universe was completely dark and the epoch lasted until the first stars and galaxies started to form and gradually reionise the universe (Wise, 2019).

Finally, with the first emerging stars and galaxies, the beginning of the Epoch of Reionisation arrived. Ionisation is the process of photons with energies higher

than 13.6 eV ionising neutral hydrogen, while creating a free electron and proton. Cosmic hydrogen reionisation is the process of ionisation of neutral hydrogen and subsequent recombination, which is a reverse action to ionisation. Thus the recombination rate must be lower than the ionisation rate for the happening of the universe reionisation.

The very early hydrogen reionisation starts when the first stars begin to form at $z \leq 30$, those are the metal-free population III (PopIII) stars (Dayal et al., 2020). For this reason the radiation from the primordial stars and early galaxies is being considered as a likely source. This first stage called the Pre-overlap stage can be seen on 1.1 and it is characterised by singular sources which ionise their immediate surroundings. Very early galaxies may have also been present at a later Pre-overlap stage, in which it was hard for the ionising photons to escape the intergalactic medium (IGM), because of its density and hence high recombination rate (Loeb, 2006). In this stage, due to the recombination the IGM is made of mostly neutral hydrogen HI regions and sparse ionised hydrogen HII regions (Zaroubi, 2013).

The second Overlap stage occurring around $z \sim 20$ to 15 as seen on 1.1 is the phase in which close ionised HII regions overlap, the IGM can be ionised by numerous sources and therefore more ionised HII regions emerge and by the end of the Overlap stage the universe is mostly ionised (Loeb, 2006). It is important to note that some sources put the beginning of reionisation era around this Overlap stage as discussed in Furlanetto et al. (2004); Zaroubi (2013); Ellis (2008).

As more galaxies formed the last and quite rapid reionisation Post-overlap stage took place (see also in 1.1). In this stage even the most dense neutral regions have been ionised along with the rising star formation in galaxies (Loeb, 2006). The universe became highly ionised for $z < 6$ and the reionisation epoch ended (Zaroubi, 2013).

The dominant sources of ionising photons are currently being discussed in numerous studies since cosmic reionisation epoch is crucial in the history of the universe for its effect on observability and star and galaxy formation (Barkana and Loeb, 2001). There are two main sources proposed, star-forming galaxies (SFGs) (reviewed by e.g., Bromm et al., 2009; Robertson et al., 2010) and quasars (e.g., Meiksin and Madau, 1993; Barkana and Loeb, 2001). Star-forming dwarf galaxies (SFDGs) were typical in this era and are therefore extensively researched for their

properties and their role in the reionisation (see section 1.2.2).

Quasi-stellar objects (QSOs), also known as quasars (first used as an abbreviation of quasi-stellar radio sources by Chiu, 1964), are the most luminous objects in the known universe. They were first discovered for their radio emission and first recognised as the nuclei of distant galaxies for their Balmer hydrogen lines by Schmidt (1963). Succeeding research on quasars placed them at the high luminosity end of the large class of Active Galactic Nuclei (AGNs). The energy source of quasars and other AGNs is the gas accretion onto super-massive black holes (SMBHs) (e.g., Hoyle and Fowler, 1963; Salpeter, 1964). The study of AGNs in the context of the Epoch of Reionisation is vital, since they are more effective than stars in the ionisation of hydrogen, and their common existence in the primordial dwarf galaxies would change the view of the history of reionisation (Barkana and Loeb, 2001).

The contribution to reionisation of both SFGs and AGNs largely depends on their UV escape fractions, which is the fraction of ionising radiation escaping the galaxy into the IGM (Zaroubi, 2013; Wise, 2019).

The contribution of the accretion radiation from AGNs remains an open question with multiple studies proposing AGNs only have a minor role in reionisation (Onoue et al., 2017; Parsa et al., 2018), but also many stating that a significant contribution is possible (Mitra et al., 2015, 2018; Grazian et al., 2018; Finkelstein et al., 2019), which seems to be accurate mainly for $z > 8$ (Dayal et al., 2020). AGNs can also be considered indirectly influence the reionisation process (Kakiichi et al., 2018). Research considering AGN jets have also been conducted, proposing that jets may have been a contribution to reionisation in two ways. Firstly, the jets of the first micro-quasars are proposed to have accelerated the energetic cosmic rays (Tueros et al., 2014; Douna et al., 2018). Secondly, the ionising photons originating in AGN jet lobes may have heated the IGM and contributed to the ionisation as well (Bosch-Ramon, 2018), with Torres-Albà et al. (2020) proposing the contribution may have been as high as $\gtrsim 10\%$ of that of star-forming galaxies.

1.2   Star-forming galaxies

1.2.1   Star formation

The process when new stars emerge from the large clouds of gas and dust in the interstellar medium (ISM) of galaxies is called star formation. When studying galaxies the star formation is the gravitational collapse of such dense clouds into star clusters.

The molecular clouds where star formation predominantly occurs are cold ($T \sim 10$ K) with high column density. These clouds are mostly composed of molecular gas hydrogen H_2, helium He, smaller amounts of atomic HI and other elements. Hydrogen tends to be molecular due to the high densities and dust particles present in the clouds and it makes direct observations of the star-forming clouds difficult (Krumholz, 2011).

Gas clouds as well as star clusters can move and collide in the ISM. The collisions have different characteristics. Due to the shortness of the mean free path between gas particles, the collision of two gas clouds brings about the conversion of the cloud bulk kinetic energy into thermal gas particle energy and consequent radiation cooling. Conversely when two star clusters collide there's essentially no possibility of a collision of two individual stars (Ward-Thompson and Whitworth, 2011).

To study the collapse of the interstellar gas clouds it is vital to take into consideration the question of their stability. In the classical case only two forces are considered - gravity, which causes the contraction of the cloud, and thermal pressure, which forces the cloud to disperse again. The occurrence of a collapse then depends on the critical initial Jeans mass and the size of the cloud (Schulz 2005). Observations have shown that magnetic and rotational effects on molecular clouds also need to be taken into account (e.g., Schulz, 2005; Ward-Thompson and Whitworth, 2011).

Star formation can be approximately constant or experience changes over time - short-lived bursts of powerful star formation (starbursts) followed by longer quiescent periods. Therefore the star formation rate (SFR) is vital for the research on the stellar content and evolution of galaxies.

For a better understanding on the significance of star formation in a given

galaxy the specific star formation rate (sSFR) is readily used (e.g., Guzmán et al., 1997; Brinchmann and Ellis, 2000). The sSFR is defined as SFR per unit stellar mass (SFR/M_*) and it is proportional to the ratio of the current SFR to the averaged over the past (Kennicutt, 1998; Orlitová, 2020). This quantity is also an interesting look into the hypothetical star formation history, since the inverse of the sSFR is the time it would take the galaxy mass to form with a constant SFR (Schneider, 2015). The sSFR also allows for better comparisons between star formation in different galaxies, since when a massive galaxy is considered, the SFR can be larger only due to the amounts of cold gas clouds in the ISM, where star formation takes place (Orlitová, 2020).

1.2.2 Star-forming dwarf galaxies

Dwarf galaxies are the most common type of galaxies in the nearby universe (e.g., Karachentsev et al., 2004). They are characterised by average low mass and metallicities and are therefore thought to be good local analogues to the galaxies in the early universe, which didn't have the time to be enriched by metals. The study of such analogues to high-redshifted galaxies, which cannot be researched without considerable errors, is crucial for the understanding of their role in the cosmic reionisation as discussed in section 1.1.

Most of the local star-forming dwarf galaxies are undergoing quiescent star formation and only a fraction are experiencing starbursts (Brinchmann et al., 2004; Lee et al., 2009). By contrast in the early universe SFDGs and especially starburst galaxies were quite frequent, which is apparent from the increase of SFR with increasing redshift (Cram et al., 1998).

There are other galaxy properties that differ from local analogues to early galaxies. One example would be the high gas content of high redshift SFDGs, which reaches up to a gas-mass fraction of 50 %, compared to the local group, where it is mostly below 30% (Schneider, 2015).

Starburst galaxies are characterised by a very intense phase of star formation. In massive galaxies the star formation is usually localised in and around the centre of the galaxy, by contrast in global starbursts occur in dwarfs (Ward-Thompson and Whitworth, 2011; Orlitová, 2020).

Although the exact mechanisms behind the powerful star formation in star-

bursts are not yet determined, most starbursts appear to be driven by gravitational interactions, including merges, of galaxies (e.g., Duc and Mirabel, 1994; Ellison et al., 2008). The interactions of the galaxies manifest as tidal forces, which allow for infall of gas towards the galaxy centre. The gas which accumulates near the galaxy centres is vital for feeding of the AGN.

The activity in star-forming and starburst galaxies can be observed by numerous methods, which were reviewed by e.g., Kennicutt and Evans (2012) and Orlitová (2020) and references therein.

Ultraviolet (UV) radiation is a typical emission coming from star-forming galaxies (SFGs), as it is typical for the massive stars in young stellar populations (namely the O and B type stars). Those stars have short lifetimes and emit hydrogen ionising far-UV (FUV) radiation at Lyman continuum wavelengths ($\lambda <$ 912 Å), which is then mostly absorbed by the ISM or the intergalactic medium (IGM). When the FUV spectrum is measured, a Lyman break appears and can be used for redshift determination or as an SFR indicator.

Lyman-break analogues (LBAs) are locally rare galaxies, which were selected to have similar high FUV luminosities with the high-redshifted Lyman-break galaxies. The LBAs are compact, starburst galaxies with sub-solar gas-phase metallicities ($12 + \log(O/H) < 8.69$, Allende Prieto et al. 2001) and they have been studied extensively (e.g., Basu-Zych et al., 2013b, 2016; Brorby et al., 2016).

After the absorption of the FUV light in the ISM or IGM, recombination can occur and emission lines form. One such line is the bright and optically thick Lyman-Alpha (Lyα) line ($\lambda = 1215.6$ Å).

Blue Compact Galaxies (BCGs), sometimes referred to as HII galaxies, are low mass ($< 10^9 M_\odot$) and low metallicity (e.g., Marconi et al., 1994; Kunth and Östlin, 2000) star-forming galaxies with bright optical emission lines. They were suggested by Kunth and Östlin (2000) as local analogues to the early, metal-deficient, galaxies, and later studied by e.g., Brorby et al. (2014). Due to their low dust content, they were expected to have a bright Lyα emission, but that has since been disproved (Kunth et al., 1998).

Green Peas (GPs) are local compact star-forming dwarf galaxies, which were discovered by the Galaxy Zoo project (Cardamone et al., 2009) and they have been named after their green appearance, caused mainly by their bright [O III]

$\lambda 5007$ emission line. There is a clear overlap between GPs and LBAs and more-over strong Lyα lines have also been observed in their emission spectra (e.g., Henry et al., 2015; Orlitová et al., 2018), pointing to them being similar to high-redshifted starburst galaxies called Lyman-Alpha Emitters (LAEs).

As star formation takes place in large clouds of gas and dust, UV emission absorption by dust and subsequent re-emission in the infrared (IR) needs to be considered. Considerable amounts of dust in star-forming galaxies make Luminous infrared galaxies (LIRGs) extremely faint in the optical and UV and instead bright in IR, although it is important to note that despite the dust contents in some LIRGs an Lyα emission was detected (Leitherer et al., 2013). The LIRGs can have a truly vigorous and mostly short-lived star formation up to SFR~ 1000 M$_\odot$yr^{-1} and so they are very active (e.g., Lehmer et al., 2010).

1.2.3 Optical classification of SFGs vs. AGNs

Optical emission lines are another characteristic of a star-forming galaxy. They are typically bright and can be formed in the ionised ISM by recombination (e.g., hydrogen Balmer series) or excitation and subsequent de-excitation (forbidden lines). When those lines are combined it allows for spectral classification between star-forming galaxies, AGNs and composites using the BPT diagram by Baldwin et al. (1981). This diagnostic typically uses the oxygen [O III] $\lambda 5007$ line, which is bright in low-metallicity and high-excitation regions (like in AGNs), and the nitrogen [N II] $\lambda 6583$ line, which differentiates between an AGN and a starburst, since its bright mostly due to an AGN.

The BPT diagram compares the [O III]/Hβ and [N II]/Hα ratios with a theoretical classification curve by Kewley et al. (2001), represented by the red line in Figure 1.2, and a revised empirical classification curve by Kauffmann et al. (2003a), shown as the blue line in Figure 1.2. The demarcation line by Kewley et al. (2001) is thought to be a lower limit on AGNs. The galaxies which fall below this line are star-forming and every galaxy above the line is a certain AGN, since similar emission lines cannot be explained for star-forming galaxies Kauffmann et al. (2003a). The empirically revised line by Kauffmann et al. (2003a) is a demarcation between composite objects and purely star-forming galaxies.

It must be pointed out that the classification by a BPT diagram is not a guaranteed way to differentiate between star formation dominated galaxies and
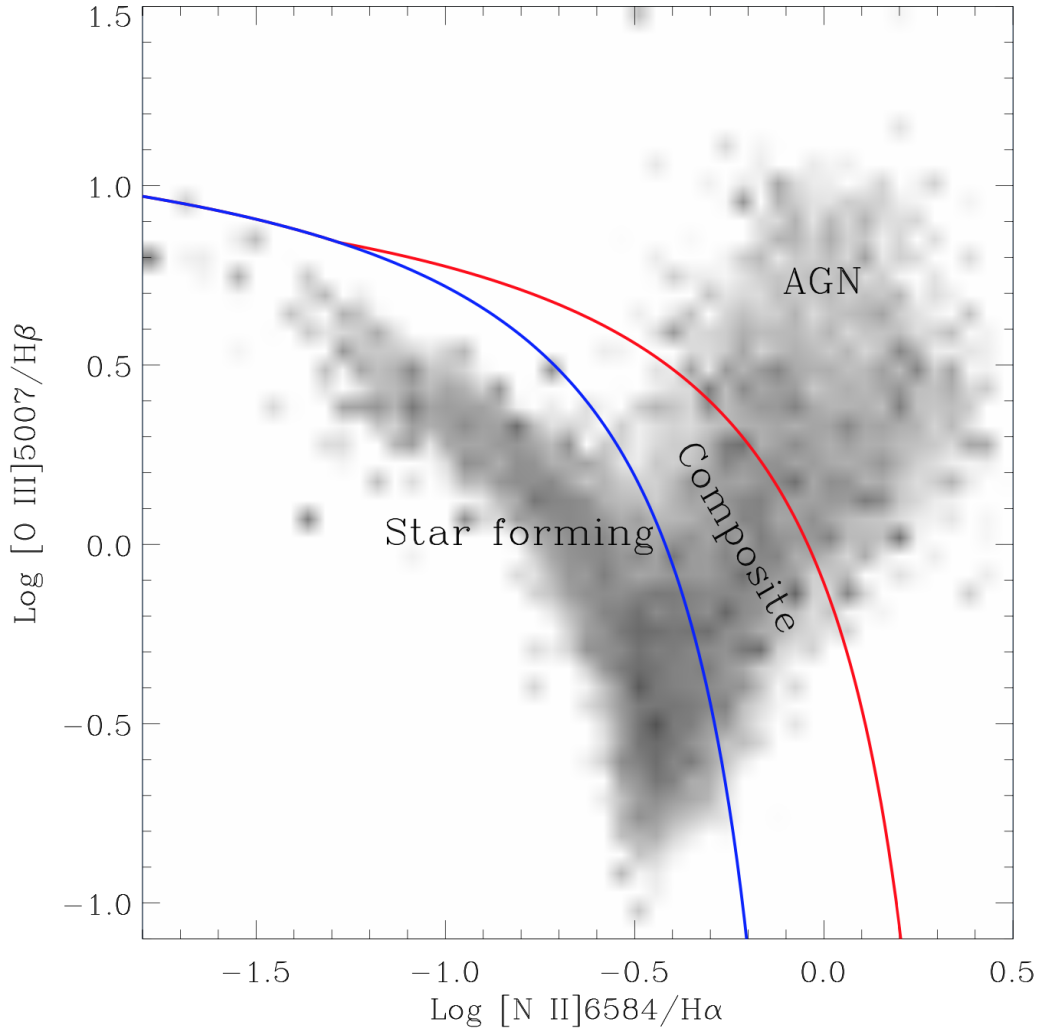
Figure 1.2: An example of a BPT (Baldwin et al., 1981) diagram, which plots the [O III]/Hβ to [N II]/Hα ratio for a sample of galaxies by Brinchmann et al. (2004). The red curve shows the classification line by Kewley et al. (2001) and the blue curve shows the revised classification line by Kauffmann et al. (2003a). Adopted from Brinchmann et al. (2004).

AGNs. Research shows, that in extreme starbursts the emission line fluxes from star formation can be as strong as in AGNs (Kewley et al., 2013). Furthermore Birchall et al. (2020), which will be further discussed in section 1.3.4, concluded that some local dwarf galaxies, classified as purely star-forming by the BPT analysis, show an excess in X-ray emission pointing towards them hosting an AGN. This result in accordance with an earlier research by Moran et al. (2002) presenting that emission from lower luminosity AGNs can be obscured by emission from the high star formation in blue and star-forming galaxies. In addition the recent research by Cann et al. (2021) presented a low metallicity dwarf galaxy, which is classified as star-forming, but shows strong evidence it hosts an AGN.

1.2.4 Metallicity

In astrophysics, metallicity is the abundance of heavier elements than hydrogen or helium. Emission lines are used to estimate abundances in star-forming galaxies. In the ISM oxygen is the most abundant element, showing very strong lines in the optical. Therefore the gas-phase oxygen abundance $12 + \log(\mathrm{O/H})$ serves as metallicity indicator, where O/H is the ratio of oxygen to hydrogen. Hereafter we use the term metallicity as identical to the gas-phase oxygen abundance.

To understand the galaxy chemical evolution in detail it is vital to study the impact of galactic winds driven by stellar feedback in star-forming galaxies (see a review by Zhang, 2018). Since the galactic winds can heat the gas in the ISM, which prevents cooling of the gas, the star formation can also be subsided as a result (Heckman et al., 2000; Bertone et al., 2007). Galactic winds are proposed to be the primary source of metals in the IGM (e.g., Aguirre et al., 2001, 2008). Their influence can therefore be evaluated by the study of metallicities of galaxies and the mass-metallicity relation.

Since measuring galaxy mass poses more difficulties than measuring luminosity, the relation between luminosity and metallicity has been studied extensively since the pioneering work by Lequeux et al. (1979). This relation has been explored for both spiral (e.g., Garnett and Shields, 1987) and irregular (e.g., Skillman et al., 1989) galaxies. Tremonti et al. (2004) has also explored this relation for a sample of star-forming galaxies from the Sloan Digital Sky Survey (SDSS) and have found a relation between metallicity and B-band luminosities:

$$12 + \log(\mathrm{O/H}) = -0.185(\pm 0.001)M_B + 5.238(\pm 0.018), \qquad (1.1)$$

where M_B is the B-band luminosity of the galaxy. Similar results have been obtained for a large sample of BCGs by Guseva et al. (2009).

Since several methods have been developed for measuring stellar mass the mass-metallicity relation has also been widely examined. Tremonti et al. (2004) have explored the mass-metallicity relation using the method of Kauffmann et al. (2003c) for stellar mass determination. This method uses spectral stellar age indicators and the fraction of new stars from recent bursts, which is an appropriate technique for the star-forming galaxies. The mass-metallicity relation as found

by Tremonti et al. (2004) is as follows:

$$12 + \log(\mathrm{O/H}) = -1.492 + 1.847(\log M_*)$$
$$= -0.08026(\log M_*)^2, \qquad (1.2)$$

where M_* is the stellar mass, with a constraint on stellar mass being $8.5 < \log M_* < 11.5$. This relationship is in agreement with other studies (e.g., Baldry et al., 2008; Davé et al., 2017) stating that galaxy metal loss is anti-correlated with stellar mass.

1.3 X-ray emission of dwarf galaxies

1.3.1 L_{X}-SFR relations

X-ray emission provides another tracer of the SFR activity. As reviewed by Orlitová (2020) in star-forming galaxies the X-ray flux comes predominantly from X-ray binaries - binary systems consisting of a main-sequence star and a compact remnant, such as a stellar mass black hole or a neutron star. Based on the mass of the donor star, the X-ray binaries are classified as high-mass X-ray binaries (HMXBs) or low-mass X-ray binaries (LMXBs).

The total X-ray emission from a galaxy is composed of the emission from HMXBs and LMXBs, hot gas from galactic winds, supernovae and their remnants. Other possible X-ray sources, which could contribute to the flux, are AGNs, driven by accretion onto compact supermassive black holes, ultra-luminous X-ray sources (ULXs), whose origin is still currently being researched (Kaaret et al., 2017), or even intermediate-mass black holes (IMBH).

In star-forming galaxies the dominant contribution to the hard X-ray luminosity (E > 2 keV) is provided by the HMXBs, which are thought to form from O and B type stars rapidly after starbursts and are short-lived (e.g., Fragos et al., 2013). The X-ray luminosity coming from HMXBs is expected to scale with SFR (Lehmer et al., 2010).

By contrast LMXBs tend to form later after a starburst and evolve slower, therefore they provide the X-ray emission mostly after the extinction of their high-mass counterparts. Their X-ray luminosity scales with the stellar mass of the galaxy (Lehmer et al. 2010).

Since total 2-10 keV X-ray luminosity from galaxies can be quantified as the

combination of contributions from HMXBs and LMXBs (Colbert et al., 2004), it is predicted that galaxies where HMXBs dominate will have a larger sSFR (SFR/M_*) than where LMXBs dominate (Lehmer et al., 2010).

Ionised hot gas, heated by the galactic winds, can according to Mineo et al. (2012b) contribute significantly (up to a third) to the 0.5 - 2 keV X-ray luminosity and scales with SFR as:

$$L_{\text{gas}} \approx (8.3 \pm 0.1) \times 10^{38} \text{ SFR}. \tag{1.3}$$

The X-ray luminosity from star-forming galaxies has been shown to be proportional to the SFR (Ranalli et al., 2003; Mineo et al., 2012a; 2014). Mineo et al. (2014) studied the X-ray luminosity of unresolved local sources and they obtained SFR relation:

$$L_{\text{XRB}}^{0.5-8\text{keV}} = (4.0 \pm 0.4) \times 10^{39} \text{ SFR}. \tag{1.4}$$

(Lehmer et al., 2016) obtained L_X-SFR relation by a different approach, taking into account galaxy's stellar mass M_*, redshift z and SFR. The relation is as follows:

$$L_{\text{XRB}} = \alpha_0(1+z)^\gamma M_* + \beta_0(1+z)^\delta \text{ SFR}, \tag{1.5}$$

where $\log_{10}(\alpha_0) = 29.04 \pm 0.17$, $\gamma = 3.78 \pm 0.82$, $\log_{10}(\beta_0) = 39.38 \pm 0.03$ and $\delta = 0.99 \pm 0.26$ for $0.5 - 2$ keV and $\log_{10}(\alpha_0) = 29.37 \pm 0.15$, $\gamma = 2.03 \pm 0.60$, $\log_{10}(\beta_0) = 39.28 \pm 0.03$ and $\delta = 1.31 \pm 0.13$ for $2 - 10$ keV.

1.3.2 L_X-SFR-metallicity relation

As the X-ray luminosity is dominated by the contribution from HMXBs, it is crucial to research the HMXB populations in relation to metallicity and redshift. The HMXBs could have had a critical role in the reionisation epoch (e.g., Jeon et al., 2014; Knevitt et al., 2014), briefly reviewed in section 1.1, and especially so if their populations would be more plentiful in the early universe.

Basu-Zych et al. (2013a; 2013b) studied the relationship between X-ray luminosity, SFR and variable redshift for two samples of LBAs with high sSFRs. High sSFRs are essential for in that case the HMXBs dominate the luminosities. They've discovered that L_X/SFR increases with growing redshift and concluded the redshift evolution of L_X/SFR is driven by metallicity changes in HMXBs.

In accordance with this is research by Douna et al. (2015), who investigated the dependence of X-ray luminosity of HMXBs on metallicity. Their sample consisted of local galaxies with high sSFRs. They found that HMXBs are just about ten times greater in low-metallicity galaxies ($12 + \log(\text{O/H}) < 8$) than in near solar-metallicity galaxies. Furthermore the X-ray luminosity of star-forming galaxies has also been observed to correlate inversely with metallicity by research of LBAs by Brorby et al. (2016), who found the L_X-SFR-metallicity plane in the form:

$$\log(L_X) = \log(\text{SFR}) + b \log((\text{O/H}))/(\text{O/H}_\odot)) + c, \qquad (1.6)$$

where L_X is measured in 0.5-8 keV and $b = -0.59 \pm 0.13$, $c = 39.49 \pm 0.09$. There have been other theoretical (Fragos et al., 2013) and experimental (Fornasini et al., 2020; Lehmer et al., 2021) studies conducted about the SFR-metallicity plane. The Fornasini et al. (2020) relation is similar to that of Brorby et al. (2016), but the L_X/SFR-metallicity slope is steeper. For metallicities $12+\log(\text{O/H}) > 8.2$ the Fornasini et al. (2020) relation agrees with the results of Lehmer et al. (2021), but not the theoretical one of Fragos et al. (2013). On contrary for lower metallicities the results of Lehmer et al. (2021) are in agreement with the theoretical predictions of Fragos et al. (2013), but the L_X/SFR-metallicity slope is flatter than in the relation given by Fornasini et al. (2020) or Brorby et al. (2016).

1.3.3 X-ray emission of GPs

Brorby and Kaaret (2017) have studied two of metal-deficient compact galaxies analogous to the GPs. They have compared the observed X-ray luminosity with the one predicted from the L_X-SFR-metallicity relation (Brorby et al., 2016)), using the equation 1.6, and found that the relation fits well within the observed luminosity measurements.

Conversely the work of Svoboda et al. (2019) researched three GPs in the X-ray spectra and found that in two of the three GPs there was a significant X-ray excess luminosity flux of the order of $\sim 10^{42}$. To calculate the excess flux the observed luminosity is again compared with the predicted one using relation 1.6. The high X-ray emission in two galaxies points to a possibility of the excess flux coming from an obscured X-ray source (AGN, IMBH or ULX).

1.3.4 X-ray emission of dwarf galaxies

A systematic search for X-ray selected AGNs in local dwarf galaxies was performed by Birchall et al. (2020). The predicted X-ray luminosities were estimated using the Lehmer et al. (2016) relation, equation 1.5, and the addition in the form of the X-ray luminosity from hot gas from Mineo et al. (2012b), equation 1.3. From a sample of about four thousand dwarf galaxies only 61 were observed with sufficient excess in the X-rays.

Optical emission lines were also used for observation, as the authors have plotted the BPT diagram ratios. They have found that only a fraction of the galaxies selected by them are showing as an AGN on the diagram, rest is classified as purely star-forming. Birchall et al. (2020) have also calculated the growth rates of the black holes and the AGN fractions were also determined.

They have used a different classification of AGNs to those relying on the BPT analysis, as they have applied their X-ray excess criterion:

$$\frac{L_{\mathrm{X-obs}}}{L_{\mathrm{XRB}} + L_{\mathrm{gas}}} \geq 3, \tag{1.7}$$

where $L_{\mathrm{X-obs}}$ is the observed X-ray luminosity, L_{XRB} is the predicted luminosity from relation by Lehmer et al. (2016), equation 1.5, and L_{gas} is the luminosity from hot gas by Mineo et al. (2012b), equation 1.3. They have used the sum of L_{XRB} and L_{gas} as their predicted X-ray luminosity, and therefore they have not included metallicity for their calculations of L_X.

In this thesis, we extend their work by considering the dependency of the X-ray luminosity on the metallicity. The results of our analysis are shown in Section 2 and discussed in Section 3. Section 4 summarises our main findings.

2. Results

We study the same sample of 61 dwarf galaxies shown as possible to host an AGN as outlined by (Birchall et al., 2020). They have used both optical and X-ray measurements to choose AGN candidates, based on their enhanced X-ray luminosity. We now consider the direct dependence of X-ray luminosity on metallicity for their sample as a possible explanation for the enhanced luminosity.

In this Section, we first describe the sample construction by Birchall et al. (2020) and their selection of AGN candidates. Next, we estimate metallicities using different methods and investigate whether the enhanced X-ray luminosity cannot be explained by the metallicity. For this purpose, we construct the L_X-SFR-metallicity plane for the studied sample and compare with other star-forming galaxies. Finally, we also compare the L_X predictions using different methods to calculate them.

2.1 Galaxy sample construction

We will now briefly describe the construction of the studied dwarf galaxy sample done by Birchall et al. (2020). They have first isolated dwarf galaxies from the Sloan Digital Sky Survey (SDSS) [1] value-added catalogue MPA-JHU[2], using SDSS Data Release 7 and 8 (DR7, DR8). The SDSS is a multi-spectral imaging and spectroscopic survey, which has produced the most detailed 3D maps of the universe and first began regular operations in 2000. SDSS uses a 2.5-m f/5 modified Ritchey-Chrétien telescope (see Gunn et al., 2006 for the technical description of the telescope), situated in New Mexico. There have been several phases of the SDSS and the next Data Release (DR17 from the SDSS-IV phase) is scheduled for July 2021, which will include a subprogram targeting the X-ray sources from X-ray focused surveys.

The MPA-JHU is a catalogue containing the derived galaxy properties estimations, such as emission line flux, redshift z, SFR (method adopted from Brinchmann et al. 2004) and stellar mass M_*. The stellar masses provided by the catalogue are estimated using method based on but not identical to Kauffmann

---

[1] https://www.sdss.org
[2] Available at: https://wwwmpa.mpa-garching.mpg.de/SDSS/DR7/

et al. (2003b). The models from Bruzual and Charlot (2003) are used and the likelihood distribution for the stellar masses is obtained. Birchall et al. (2020) defined a dwarf galaxy as having stellar mass $M_* \leq 3 \times 10^9 \ M_\odot$ and they have applied this criterion on the galaxy sample from the MPA-JHU catalogue, which yielded $\sim$65 000 galaxies. Since the MPA-JHU only contains objects classified as galaxies by the SDSS, they have also searched in the SDSS DR7 quasar catalogue by Shen et al. (2011), but none were found according to their criteria.

Next, the X-ray data from the 3XMM DR7 catalogue by Rosen et al. (2016) were used. The catalogue is based on the observations from the European Space Agency's (ESA) X-ray Multi-Mirror Mission (XMM-Newton)[3]. The XMM is a space-based observatory used for spectroscopic measurements of X-rays, that can only be measured by detectors in space due to the Earth's atmosphere blocking of them. It uses three X-ray telescopes with unparalleled effective area and an Optical Monitor. Birchall et al. (2020) matched the optical positions from the entire MPA-JHU catalogue to those of the X-ray sources from the 3XMM, using a radius of 10" around them, which resulted in $\sim$3000 matches. They have used the sum of the measured 2 - 4.5 keV and 4.5 - 12 keV fluxes and converted them to the 2 - 12 keV energy band.

Using the previous $\sim$3000 X-ray source matches, Birchall et al. (2020) calculated the position-error-normalised separation $x = d_{O,X}/\Delta_X$, where $d_{O,X}$ is the separation between X-ray and optical signals, Δ_X is the X-ray position error, for each dwarf galaxy and X-ray source pair. They considered the sources a match only if $x < 3.5$ and following Rosen et al. (2016) limited the X-ray source to 10". After matching this with the dwarf galaxy sample from the MPA-JHU, 101 galaxies were obtained. Birchall et al. (2020) further investigated these galaxies and removed 15 of them (11 due to closer high-mass galaxies, 3 as a result of optical correction and 1 for extremely high redshift error). This resulted in a 86 galaxy sample.

Using this sample, Birchall et al. (2020) compared their X-ray luminosities with luminosity predictions from the X-ray binaries (XRBs) and the possible contribution from hot gas. They have calculated the luminosity from XRBs L_{XRB} according to Lehmer et al. (2016), equation 1.5. They found that the most galaxies (76 out of 86) show the observed X-ray luminosity larger than

---

[3]https://sci.esa.int/web/xmm-newton/

Name	Abbr. Name	Redshift	SFR $(M_\odot \text{ yr}^{-1})$	Mass M_* $(M_\odot)$	$L_{\text{X-obs [2-12 keV]}}$ (erg s^{-1})		
SDSS J011523.96+003808.7	J0115+0038	0.0352	1.39E-01	8.60E+08	4.90E+40	±	5.1E40
SDSS J014529.26+001036.0	J0145+0010	0.0805	3.61E-01	1.14E+09	7.77E+40	±	6.4E40
SDSS J024117.09-001352.3	J0241-0013	0.0308	2.85E-01	1.70E+09	4.71E+39	±	7.7E39
2MASX J02564580+0603173	J0256+0603	0.0262	3.21E-02	3.09E+06	3.41E+39	±	1.9E40
LEDA 2402319	LEDA 2402319	0.0392	6.57E-01	2.82E+09	3.19E+40	±	4.1E40
2MASX J08193880+2103521	J0819+2103	0.0141	5.00E-02	1.12E+09	2.69E+39	±	4.8E39
SDSS J082228.93+034551.7	J0822+0345	0.0351	1.30E+00	6.63E+08	1.13E+40	±	4.9E39
2MASS J08320052+1912058	J0832+1912	0.0375	1.61E+00	1.97E+09	4.16E+40	±	1.8E40
SDSS J085629.97+380456.1	J0856+3804	0.0400	2.85E-01	1.04E+09	7.70E+39	±	1.4E40
SDSS J090335.40+151142.0	J0903+1511	0.0288	6.70E-02	7.49E+08	1.46E+40	±	9.8E39
SDSSCGB 15.2	SDSSCGB 15.2	0.0338	2.50E+00	1.57E+09	4.24E+40	±	2.9E40
2XMMi J092720.4+362407	J0927+3624	0.0190	1.13E-01	3.30E+08	7.88E+39	±	3.7E39
PWC2011 J100805.1+125650	J1008+1256	0.0317	3.53E-01	2.46E+09	1.93E+40	±	1.3E40
SDSS J102526.59+124540.3	J1025+1245	0.0309	3.28E-01	1.02E+09	8.44E+39	±	1.7E40
LEDA 30866	LEDA 30866	0.0368	3.90E-01	8.41E+07	3.12E+39	±	2.4E40
Mrk 1434	Mrk 1434	0.0075	6.15E-02	1.00E+07	1.18E+40	±	3.0E39
SDSS J103844.88+533005.2	J1038+5330	0.0032	2.19E-01	3.84E+07	3.78E+39	±	2.4E38
LEDA 2116718	LEDA 2116718	0.0290	1.57E-01	4.15E+08	3.11E+39	±	2.3E40
UGC 6192	UGC 6192	0.0068	5.04E-02	2.43E+08	1.60E+39	±	4.2E38
SDSS J112830.77+533005.2	J1128+5330	0.0100	5.87E-01	1.67E+09	4.01E+40	±	5.5E39
SDSS J112910.56+582309.0	J1129+5823	0.0411	1.17E+00	1.28E+09	2.99E+40	±	3.4E40
Mrk 1303	Mrk 1303	0.0220	1.10E+00	8.35E+08	1.06E+40	±	6.7E39
2XMM J114501.7+194549	J1145+1945	0.0274	8.60E-02	2.27E+09	1.02E+40	±	7.2E39
SDSS J115558.40+232730.7	J1155+2327	0.0521	1.43E+00	2.14E+09	3.80E+40	±	2.1E40
NGC 4117	NGC 4117	0.0032	1.70E-02	2.18E+09	6.17E+39	±	5.0E38
ECO 11516	ECO 11516	0.0236	1.10E-01	1.92E+09	2.21E+40	±	1.3E40
SDSS J121352.97+141312.5	J1213+1413	0.0247	3.28E-01	1.11E+09	3.36E+39	±	8.5E39
SDSS J121707.89+034056.3	J1217+0340	0.0069	5.30E-02	1.05E+07	2.24E+39	±	1.4E39
LEDA 39539	LEDA 39539	0.0076	1.90E-03	2.17E+08	2.47E+39	±	1.3E39
NGC 4395	NGC 4395	0.0011	1.57E-04	2.50E+07	1.39E+40	±	7.0E38
2XMM J123519.9+393110	J1235+3931	0.0209	2.60E-01	7.85E+07	1.10E+40	±	4.4E39
NVSS J123542-001252	J1235-0012	0.0234	4.15E-01	6.47E+07	7.14E+39	±	9.3E39
LEDA 44693	LEDA 44693	0.0228	2.22E-02	1.73E+09	8.02E+39	±	6.0E39
7W 1258+27W06	1258+27W06	0.0250	1.04E+00	2.64E+09	2.45E+40	±	2.3E40
2MASX J13070847+5357446	J1307+5357	0.0294	2.20E+00	2.37E+09	4.89E+40	±	3.3E40
SDSS J130821.42+113055.0	J1308+1130	0.0250	2.17E-01	2.03E+08	4.99E+39	±	1.5E40
SDSS J131930.27+552146.0	J1319+5521	0.0235	2.72E-01	1.09E+09	7.34E+39	±	6.0E39
2XMM J134107.9+263047	J1341+2630	0.0703	1.22E+00	2.50E+09	5.54E+40	±	1.2E41
2XMM J134427.6+560130	J1344+5601	0.0706	1.60E+01	1.40E+09	1.57E+41	±	8.2E40
2XMM J134719.1+581437	J1347+5814	0.0348	5.08E-01	1.26E+09	1.23E+40	±	5.5E39
2XMM J134736.4+173404	J1347+1734	0.0447	1.26E+00	2.28E+09	8.88E+41	±	5.9E40
UGC 9215	UGC 9215	0.0047	2.17E-01	6.87E+08	3.85E+39	±	1.6E39
SDSS J143102.57+281625.9	J1431+2816	0.0318	3.14E-01	9.17E+08	8.26E+39	±	9.3E39
2MASX J14401271+0247441	J1440+0247	0.0299	7.20E-01	2.66E+09	2.42E+40	±	8.1E39
2XMM J144056.3+033145	J1440+0331	0.0338	1.42E-01	1.44E+08	4.34E+39	±	8.9E39
ECO 2050	ECO 2050	0.0223	1.33E-01	4.27E+08	2.07E+39	±	4.8E39
SDSS J153704.18+551550.5	J1537+5515	0.0022	2.46E-02	7.24E+06	1.13E+39	±	1.8E38
SDSS J154818.94+350741.2	J1548+3507	0.0552	5.82E-01	1.66E+09	7.10E+39	±	1.4E40
2XMM J160531.8+174825	J1605+1748	0.0317	1.53E-01	1.64E+09	6.91E+40	±	3.2E40
AGC 262533	AGC 262533	0.0093	4.94E-02	1.64E+08	3.16E+39	±	9.4E38
SDSS J161321.26+510534.8	J1613+5105	0.0336	6.25E-01	1.57E+09	1.09E+40	±	2.0E40
SDSS J162642.49+390842.8	J1626+3908	0.0283	3.90E-01	7.65E+08	3.04E+40	±	1.4E40
SDSS J162729.77+385455.1	J1627+3854	0.0324	2.53E-01	1.08E+09	1.60E+40	±	1.8E40
SDSS J213732.54+002800.1	J2137+0028	0.0528	2.56E-01	6.87E+08	3.95E+39	±	8.9E39
SDSS J213743.69+003125.5	J2137+0031	0.0524	1.87E-01	1.19E+09	2.34E+40	±	2.2E40
6dFGS gJ233225.3-005049	gJ2332-0050	0.0176	3.65E-01	8.26E+08	1.35E+40	±	9.8E39
SDSS J011421.73+001335.6	J0114+0013	0.1319	2.71E-02	1.92E+09	1.59E+41	±	6.2E41
SDSS J012325.32-002921.4	J0123-0029	0.0286	1.14E-03	8.53E+08	5.02E+39	±	1.3E40
SDSS J030446.14-011208.1	J0304-0112	0.0144	4.85E-04	1.52E+08	5.66E+40	±	2.6E40
SDSS J220558.60-003049.3	J2205-0030	0.0821	2.11E-02	2.92E+09	1.27E+41	±	8.6E40
SDSS J234759.26+010344.2	J2347+0103	0.2465	7.23E-02	1.27E+09	5.35E+42	±	5.2E42

Table 2.1: Birchall et al. (2020) 61 X-ray active dwarf galaxy sample. Redshift z and stellar mass M_* taken from the MPA-JHU catalogue, as well as SFR for the first 56 galaxies. For the last 5 galaxies SFR, was calculated by the method of Kennicutt and Evans (2012). The observed 2 - 12 keV X-ray luminosity is taken from 3XMM.

the predicted value L_{XRB}. Next, they have taken the contribution from hot gas into account and summed the L_{XRB} with the X-ray luminosity from hot gas L_{gas} derived by Mineo et al. (2012b), equation 1.3, to obtain their new estimate of the predicted X-ray luminosity. The predicted emission from the hot gas was negligible and they have found the same 76 galaxies with an X-ray excess flux. Before accepting this sample they have applied their X-ray excess criterion, equation 1.7 (see Section 1.3.4), and made the final X-ray active dwarf galaxy sample with 61 galaxies showing a possibility to host an AGN. The properties of this galaxy sample are shown on Table 2.1, including redshift z, SFR, stellar mass M_* and the observed 2 - 12 keV X-ray luminosity $L_{\mathrm{X-obs}}$.

2.2 Galaxy metallicity analysis

Birchall et al. (2020) have not considered metallicity directly in their analysis, although it can have an impact on the X-ray luminosity from XRBs. We therefore used the MPA-JHU catalogue to constrain the metallicity for all galaxies in the studied sample and we employed different methods for galaxy metallicity estimations. Then, we compared our metallicities with the values in the MPA-JHU catalogue.

The MPA-JHU catalogue uses the Bayesian method outlined by Tremonti et al. (2004) and Brinchmann et al. (2004) for their metallicity estimations. As discussed in detail by Tremonti et al. (2004) this method (hereafter M-J) estimates metallicities statistically, fitting all the prominent emission lines (H$_\alpha$, H$_\beta$, [OII], [OIII], [NII], [SII]) simultaneously. This methodology has the advantage of full spectral modelling using all the available emission lines. For that reason we consider this method the most accurate, albeit Tremonti et al. (2004) omitted galaxies considered as AGNs by the BPT diagnostic (Baldwin et al., 1981; classification by Kauffmann et al., 2003a) from their modelling. As previously discussed in Section 1.2.3, there is some uncertainty in the BPT diagnostics of the AGN vs. SFG, and so it might be well possible that some obscured AGNs may have been present in the sample used for metallicity estimates.

Since the M-J statistical method cannot be used universally for all galaxy samples, Tremonti et al. (2004) also provides analytical fit (hereafter TR04) using

the $R_{23} = ([OII]\lambda3727, \lambda3729 + [OIII]\lambda4959, \lambda5007)/H_\beta$ metallicity indicator:

$$12 + \log(\text{O/H}) = 9.185 - 0.313\log R_{23} - 0.264\log^2 R_{23} - 0.321\log^3 R_{23}. \quad (2.1)$$

Considering the [OII] line cannot be measured for galaxies with $z < 0.023$, due to the blue wavelength cut-off, Pilyugin and Mattsson (2011) established metallicity estimate (hereafter PI11) using the [OIII], [NII], [SII] and H_β lines in the form:

$$12 + \log(\text{O/H}) = a_0 + a_1 \log R_3 + a_2 \log N_2 + a_3 \log(N_2/S_2), \quad (2.2)$$

where $R_3 = ([OIII]\lambda4959, \lambda5007)/H_\beta$, $N_2 = ([NII]\lambda6548, \lambda6584)/H_\beta$, $S_2 = ([SII]\lambda6717, \lambda6731)/H_\beta$ and the coefficients a_0, a_1, a_2, a_3 depend on the values of $\log(N_2)$ and $\log(N_2/S_2)$.

Pettini and Pagel (2004) introduced another method (hereafter PE04) to determine metallicity estimates using the [OIII], [NII], H_α and H_β lines. They defined a quantity $O3N2 = \log(([OIII] \lambda5007/H_\beta)/([NII] \lambda6583/H_\alpha))$ and for $-1 < O3N2 < 1.9$ estimate the metallicity as:

$$12 + \log(\text{O/H}) = 8.73 - 0.32 \times O3N2. \quad (2.3)$$

We have used and compared all these methods, using the line fluxes from the MPA-JHU catalogue, and our results, along with the line fluxes, are summarised in Table 2.2. The MPA-JHU catalogue (named M-J in the table) provides us the least amount of metallicities for our galaxy sample (only 40 values were found out of 61), therefore we used these metallicities as our reference and chose a different and more fitting method. The PI11 approach provides 57 metallicities as well as the PE04 methodology and the TR04 gives only 54 estimates.

Along with the number of galaxies for which a method can be used, the mean values of metallicities also provide an effective feedback about which method is more suitable. On average, the method PI11 grants smaller metallicities than the values from MPA-JHU by 0.33, PE04 only by 0.20 and TR04 gives larger values by 0.18.

Since the PI11 brings the largest difference in mean metallicities, we decided to not use this method. It can be speculated that the difference stems from the fact this method was mainly devised for use with galaxies with $z < 0.023$ and our sample ranges $0.003 < z < 0.25$. The difference between the values from

Abbr. Name	H$_\alpha$	H$_\beta$	[OII] λ3726	[OII] λ3729	[OIII] λ4959	[OIII] λ5007	[NII] λ6548	[NII] λ6584	[SII] λ6717	[SII] λ6731	PI18	TR04	**PE04**	M-J
J0115+0038	862,30	269,11	253,87	314,03	431,17	1279,7	15,61	47,08	63,55	47,31	8,20	8,41	**8,11**	8,53
J0145+0010	363,49	106,86	116,46	138,08	153,78	460,14	6,36	19,19	34,51	19,45	8,10	8,44	**8,12**	8,25
J0241-0013	1068,4	271,25	361,57	362,19	58,58	187,66	98,23	296,27	173,45	130,64	8,43	8,88	**8,60**	8,93
J0256+0603	1678,7	464,81	481,11	589,72	633,16	1891,6	29,54	89,11	164,24	133,19	8,09	8,47	**8,13**	8,23
LEDA 2402319	102,89	31,69	26,63	58,99	8,19	23,91	8,26	24,93	30,54	16,80	8,41	8,86	**8,57**	8,66
J0819+2103	139,35	43,26	0,00	0,00	5,64	17,79	11,06	33,36	35,04	22,12	8,48	9,26	**8,65**	8,81
J0822+0345	1137,0	418,08	695,03	736,84	432,25	1282,4	29,48	88,92	173,12	118,19	8,02	8,49	**8,22**	8,24
J0832+1912	15423	549,64	666,45	594,92	365,00	6069,3	139,11	419,58	237,57	189,94	8,25	8,00	**7,90**	-
J0856+3804	63,63	17,51	38,85	37,56	7,17	22,33	2,28	6,86	17,91	11,40	7,87	8,63	**8,39**	-
J0903+1511	55,69	17,61	36,59	43,18	9,32	33,75	3,02	9,12	12,45	8,43	8,37	8,54	**8,39**	8,47
SDSSCGB 15.2	2459,8	703,87	831,91	843,02	383,32	1106,6	110,40	333,00	285,67	210,61	8,44	8,78	**8,39**	8,77
J0927+3624	182,49	67,98	0,00	0,00	37,01	115,37	6,62	19,98	33,73	27,47	8,43	9,03	**8,35**	8,30
J1008+1256	342,35	94,50	85,11	101,55	18,45	47,34	35,25	106,31	78,43	58,37	8,43	8,98	**8,66**	8,87
J1025+1245	20,10	4,31	19,69	-16,26	-6,79	2,66	7,99	24,10	5,60	2,27	-	-	**8,82**	8,68
LEDA 30866	1868,1	460,52	202,00	231,46	49,59	147,14	204,09	615,58	265,62	201,24	8,51	9,14	**8,73**	9,07
Mrk 1434	6172,5	2290,1	0,00	0,00	4055,8	11884	27,95	84,32	180,99	135,49	8,63	8,54	**7,90**	7,93
J1038+5330	0,00	24807	0,00	0,00	22515	64622	3951,2	11919	7054,9	5685,9	8,43	8,88	**-**	-
LEDA 2116718	158,69	53,22	79,51	84,99	34,99	103,63	6,74	20,32	32,56	20,84	8,39	8,66	**8,35**	8,42
UGC 6192	232,86	67,17	0,00	0,00	157,85	473,98	14,67	44,25	60,71	50,41	8,19	8,33	**8,23**	-
J1128+5330	14658	3132,0	0,00	0,00	1157,4	3576,7	1998,3	6027,3	2135,1	1833,7	8,35	9,12	**8,59**	-
J1129+5823	1397,1	372,50	518,27	555,94	282,72	832,74	53,48	161,30	202,52	150,40	8,38	8,64	**8,32**	8,62
Mrk 1303	6476,1	2166,0	-193498	302,78	1808,7	5503,3	282,21	851,23	698,63	510,13	8,43	-	**8,32**	8,70
J1145+1945	4,53	-0,05	-1,24	12,82	7,17	3,97	0,93	2,79	-3,06	1,31	-	-	**-**	-
J1155+2327	265,02	77,50	113,45	133,03	36,30	102,39	16,60	50,05	55,00	39,42	8,38	8,73	**8,46**	8,67
NGC 4117	2442,0	608,82	0,00	0,00	791,77	2424,6	333,08	1004,6	1009,1	787,83	8,14	8,70	**8,41**	-
ECO 11516	320,70	100,07	100,92	93,44	206,34	614,24	20,41	61,56	49,86	44,10	8,27	8,28	**8,25**	-
J1213+1413	1113,7	245,50	188,15	204,16	75,26	234,75	85,43	257,68	107,29	85,04	8,45	8,96	**8,53**	8,99
J1217+0340	3752,4	987,91	0,00	0,00	183,11	579,40	297,19	896,38	664,55	468,64	8,45	9,22	**8,61**	8,91
LEDA 39539	0,12	-2,96	0,00	0,00	1,94	3,18	0,12	0,36	-0,08	0,45	-	-	**-**	-
NGC 4395	13690	3375,0	0,00	0,00	10505	31628	1045,2	3152,4	2270,1	2760,3	8,16	8,10	**8,21**	-
J1235+3931	1663,0	541,85	325542	-104,66	771,78	2323,2	9,40	28,35	78,66	56,19	8,57	-	**7,96**	7,90
J1235-0012	2716,7	452,91	0,00	0,00	54,53	157,36	346,39	1044,8	448,68	333,08	8,41	9,27	**8,74**	9,05
LEDA 44693	0,92	-1,50	0,00	0,19	0,03	-0,16	0,80	2,42	0,17	-2,74	-	-	**9,17**	-
1258+27W06	1072,5	285,63	215,42	246,80	23,11	77,89	99,85	301,16	209,60	151,24	8,51	9,06	**8,73**	8,97
J1307+5357	4291,7	1186,5	1241,2	1097,0	781,43	2329,2	223,98	675,57	609,47	451,77	8,39	8,77	**8,38**	8,71
J1308+1130	805,28	280,22	300,85	345,68	326,35	967,35	12,71	38,33	87,53	62,00	8,46	8,55	**8,13**	8,02
J1319+5521	100,42	33,11	-9,2+E06	10934	14,12	41,93	6,20	18,70	27,22	13,46	8,39	-	**8,46**	8,50
J1341+2630	686,70	193,71	251,40	240,67	125,02	365,47	49,03	147,87	98,20	80,04	8,38	8,72	**8,43**	8,77
J1344+5601	6607,2	1772,1	1791,2	1409,7	2882,6	8792,3	162,84	491,16	518,36	413,16	8,39	8,42	**8,15**	8,54
J1347+5814	121,26	37,07	58,26	67,03	15,28	40,82	7,88	23,76	40,69	22,40	8,36	8,74	**8,49**	8,52
J1347+1734	765,16	223,96	378,88	433,12	565,46	1681,9	228,73	689,89	197,69	150,37	8,13	8,02	**8,44**	-
UGC 9215	1177,7	337,43	0,00	0,00	138,21	397,25	96,34	290,60	291,51	210,11	8,36	9,11	**8,51**	8,68
J1431+2816	784,46	237,60	305,77	362,47	146,90	433,37	36,91	111,33	136,31	104,61	8,39	8,70	**8,38**	8,61
J1440+0247	2782,5	758,14	782,88	447,42	1815,7	5317,6	345,97	1043,5	394,18	382,93	8,21	8,21	**8,32**	-
J1440+0331	1151,4	263,25	136,36	150,94	22,31	53,35	112,00	337,82	209,77	148,62	8,51	9,18	**8,78**	9,03
ECO 2050	43,43	14,25	0,00	0,00	2,75	12,46	1,66	5,01	14,48	7,66	8,43	9,18	**8,45**	-
J1537+5515	23109	6561,8	0,00	0,00	15290	0,00	145,65	439,32	686,29	544,60	8,67	9,02	**-**	-
J1548+3507	218,61	72,86	106,02	111,09	31,91	83,54	12,41	37,43	49,77	31,81	8,41	8,77	**8,47**	8,63
J1605+1748	163,38	44,00	17,81	14,12	15,90	52,74	14,62	44,09	18,88	14,68	8,43	9,02	**8,52**	8,96
AGC 262533	1629,4	530,77	0,00	0,00	408,13	1198,4	52,29	157,73	255,99	173,14	8,41	8,94	**8,29**	8,42
J1613+5105	103,77	28,00	47,77	59,18	10,96	33,99	6,84	20,62	28,02	21,38	8,35	8,69	**8,48**	8,56
J1626+3908	1279,4	393,51	638,04	688,51	208,12	648,43	63,04	190,14	240,04	161,29	8,40	8,67	**8,40**	8,62
J1627+3854	742,29	241,69	353,57	365,12	183,64	555,84	34,77	104,87	103,24	81,15	8,40	8,63	**8,34**	8,64
J2137+0028	37,14	11,27	8,36	11,79	1,20	13,68	1,49	4,48	10,04	5,05	8,42	8,93	**8,41**	-
J2137+0031	130,57	39,96	65,05	66,83	11,00	35,06	10,19	30,72	32,61	21,34	8,41	8,78	**8,55**	8,70
gJ2332-0050	228,94	63,40	0,00	0,00	39,33	141,06	10,59	31,94	49,11	34,93	8,34	8,96	**8,35**	8,45
J0114+0013	11,87	1,88	11,11	5,00	-0,70	6,05	3,18	9,58	1,30	6,41	8,11	8,18	**8,54**	-
J0123-0029	12,39	2,17	2,26	16,97	-1,22	4,65	0,76	2,30	4,02	-2,39	8,43	8,25	**8,39**	-
J0304-0112	21,12	4,56	0,00	0,00	3,45	10,09	0,80	2,43	5,78	-0,95	8,36	8,94	**8,32**	-
J2205-0030	25,49	7,47	10,73	14,67	2,91	9,31	1,10	3,33	5,50	157,72	8,08	8,72	**8,42**	-
J2347+0103	7,87	1,19	2,29	7,83	0,76	4,11	1,65	4,96	3,46	1,11	8,09	8,09	**8,49**	-

Table 2.2: Emission line fluxes and metallicities of the sample of Birchall et al. (2020). Emission line fluxes and M-J metallicity values are reported in the MPA-JHU catalogue. Metallicities PI11, TR04, and PE04 are calculated from the line fluxes (see the main text for more details). Method PE04 is used further for analysis and is therefore emphasised by boldface. The emission line fluxes are in the units of 1E-17 erg s^{-1} cm^{-2}.

MPA-JHU and the results from TR04 and PE04 methods are similar, and so we decided to use the PE04 approach to create our sub-sample, because not only will it give us the needed metallicities for more galaxies, but also the papers, with

which our results will be compared with, by e.g., Brorby et al. (2016); Svoboda et al. (2019) adopt it.

With PE04 method, we have the metallicity estimate for 57 out of 61 sources (see Table 2.2), which is the vast majority of the sample. From the rest 4 sources, 2 galaxies have no available metallicity estimate by any method and 2 could have an estimate from the PI11 method. But for simplicity and not introducing any systematic error, we have decided to further study only the 57 sources with the consistent metallicity estimate by PE04 method.

2.3 Dwarfs in L_{X}-SFR-metallicity plane

2.3.1 Comparison with the L_{X}-SFR plane

With our metallicity estimates, we can now study the dwarf galaxies from the Birchall et al. (2020) sample not only in the L_X-SFR plane, but also in the L_X-SFR-metallicity plane for star-forming galaxies and compare them (see Figure 2.1). The observed 2-12 keV X-ray luminosity is in units of erg/s and is taken from the work of Birchall et al. (2020), who used the values from 3XMM. We have used the SFRs (in units of $M_\odot$/yr) from the MPA-JHU catalogue for 52 galaxies and for 5 galaxies the Kennicutt and Evans (2012) H_α emission line method was used for more precise estimate, following the analysis by Birchall et al. (2020). The redshift z from the MPA-JHU catalogue was used and the metallicities were determined by the PE04 method (see Section 2.2). This creates our sub-sample of 57 galaxies from the original Birchall et al. (2020) sample of AGN candidates, which have estimated metallicities by the same PE04 method.

The shift to either left or right is distinctly visible in Figure 2.1. The dark green points correspond to the values with no metallicity used by Birchall et al. (2020) and therefore also to their Figure 5, the blue points then correspond to our values with estimations of metallicity. As the metallicities are typically sub-solar $(12 + \log(\mathrm{O/H}) < 8.69)$, the shift is mostly to the right of the diagram. It is also clearly visible the shift is not major, since for most galaxies the metallicity is not so largely different from the Solar value - the mean value of metallicity for the studied sample is $12 + \log(\mathrm{O/H}) = 8.42$. As the shift due to metallicity is not so significant, the role of metallicity is more as a correction rather than a determining factor.
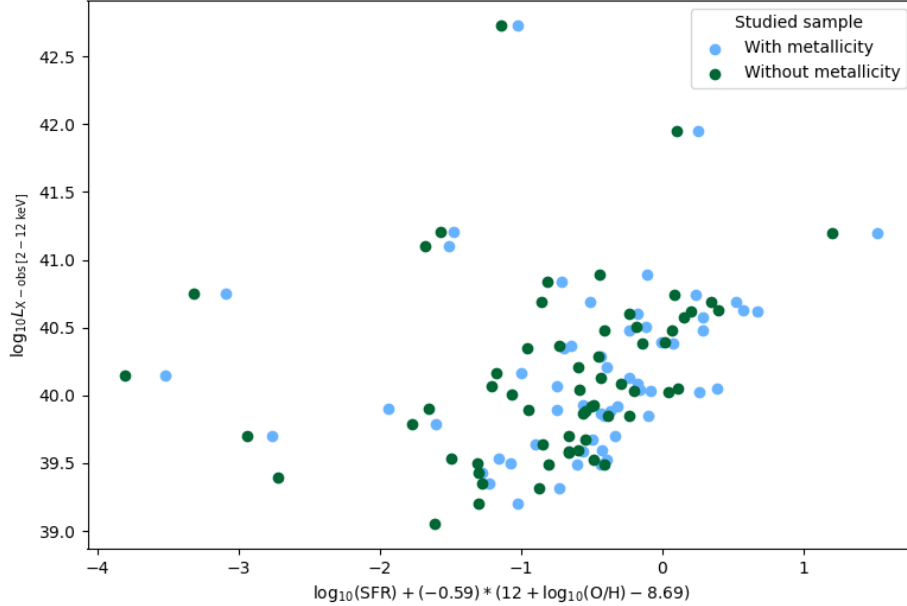
Figure 2.1: Our dwarf galaxy sample plotted in the diagram of the L_X-SFR-metallicity plane shown as the blue points. The dark green points correspond to the L_X-SFR plane, without metallicity considered as studied by Birchall et al. (2020). The observed 2-12 keV X-ray luminosity is in units of erg s^{-1}, the SFR is in units of $M_\odot$ yr^{-1}.

2.3.2 Comparison with star-forming galaxies from other samples

To compare our results with the relation by Brorby et al. (2016) derived for the L_X-SFR-metallicity plane and also with other galaxy samples of Douna et al. (2015); Brorby et al. (2016); Brorby and Kaaret (2017) and Svoboda et al. (2019), we have plotted the samples, including our sub-sample, in the L_X-SFR-metallicity plane (see Figure 2.2). The Douna et al. (2015) sample used X-ray luminosities for resolved X-ray sources and so, following the work by Svoboda et al. (2019), we applied the same correction on the Douna et al. (2015) sample so the galaxy samples can be compared. Mineo et al. (2012a) derived a L_X-SFR relation for resolved galaxies in the 0.5 - 8 keV energy band as $L_X \approx 2.6 \times 10^{39}$ SFR, Mineo et al. (2014) derived the L_X-SFR relation for unresolved sources as the total X-ray emission as $L_X \approx 4 \times 10^{39}$ SFR (see equation 1.4). Therefore to estimate the total 0.5 - 8 keV X-ray luminosity of star-forming galaxies we can apply the factor 4/2.6 to luminosity for resolved sources. The rest of the galaxy samples used unresolved X-ray emission (Svoboda et al., 2019) or applied analogous corrections (Brorby
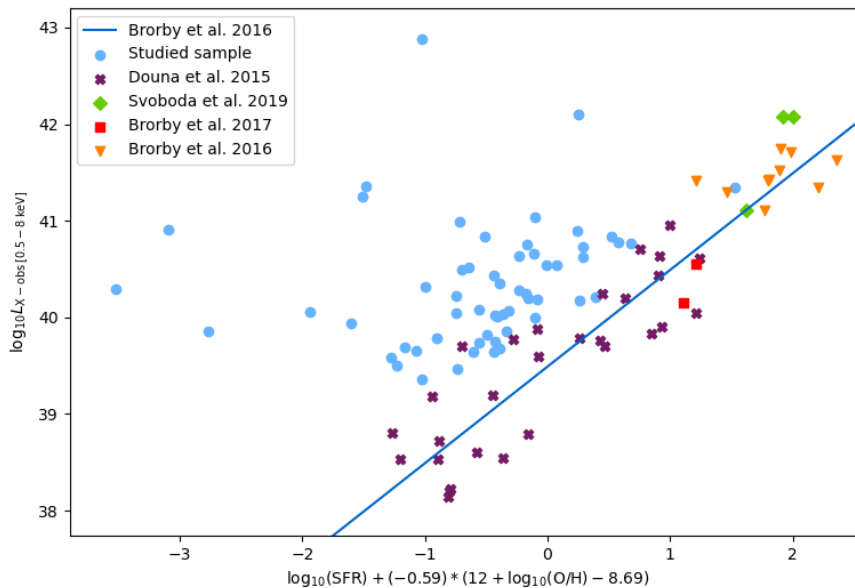
Figure 2.2: Studied dwarf-galaxy sample plotted in the L_X-SFR-metallicity plane is shown as the blue points. The purple crosses correspond to the star-forming galaxies from the Douna et al. (2015) sample. The green diamonds are the GPs from Svoboda et al. (2019). The red squares are the Green Pea analogues by Brorby and Kaaret (2017) and the orange triangles are the LBAs studied by Brorby et al. (2016). The blue line is the relation of the L_X-SFR-metallicity plane derived by Brorby et al. (2016). The observed 0.5-8 keV X-ray luminosity is in units of erg s^{-1}, the SFR is in units of $M_\odot$ yr^{-1}.

et al., 2016; Brorby and Kaaret, 2017), and they can therefore be used for direct comparison.

The studied dwarf galaxy sample has reported X-ray luminosities in the 2 - 12 keV band. In order to be compatible to the other galaxy samples and the relation by Brorby et al. (2016) we needed to convert our observed X-ray luminosities to the 0.5-8 keV band. The hard X-ray spectra of AGNs can be represented by a power law spectra in the form of $I_\nu \approx \nu^{-\alpha}$, where ν is the specific frequency and α is the spectral slope. In X-ray astronomy, it is more common to refer to the photon index $\Gamma = \alpha + 1$, to describe the power-law slope. These photon indexes have been measured for extensive AGN samples and the usual values fall in the $\Gamma \sim 1.5 - 2.5$ range, with an avarage value $\Gamma = 1.9$ (e.g., Nandra and Pounds, 1994; Piconcelli et al., 2005). As our studied galaxy sample is made up of possible hosts of AGNs, we decided to assume $\Gamma = 1.9$ and use the relation to extrapolate

the X-ray luminosities as derived in Svoboda et al. (2017):

$$F_{0.5-8\,keV} = F_{2-12\,keV} \frac{8^{-\Gamma+2} - 0.5^{-\Gamma+2}}{12^{-\Gamma+2} - 2^{-\Gamma+2}}, \tag{2.4}$$

where $F_{2-12\,keV}$ is the observed X-ray flux, which is converted to the desired $F_{0.5-8\,keV}$ flux.

As can be seen in Figure 2.2 in context of SFR and metallicity, most of our dwarf galaxy sample lies in similar region as the star-forming galaxy sample of Douna et al. (2015), with few galaxies being lower in SFR and metallicity. Concerning the X-ray luminosity, however, our sample is found to be significantly higher in the diagram. The studied sample overall seems to be superior to other galaxy samples in terms of the X-ray luminosity, with most of our galaxies lying above the line by Brorby et al. (2016), shown as the blue line in Figure 2.2. This clearly indicates an X-ray excess emission compared with the sample of Brorby et al. (2016) used to derive the relation. For the points on the far left side of the diagram the relation would predict luminosities lower by a several orders of magnitude.

2.3.3   Specific star formation rate relations

We have previously stated, that the sSFR (SFR/M$_*$) is a better quantity regarding the determination of the influence the SFR has in a given galaxy and also for comparison between different galaxies and their samples. The total 2-10 keV X-ray luminosity is the sum of luminosities form HMXBs and LMXBs and Lehmer et al. (2010) derived the relation in the form of:

$$L_{X\,(2-10\,\text{keV})}/\text{SFR} = \alpha/(\text{sSFR}) + \beta, \tag{2.5}$$

where $\alpha = (9.05 \pm 0.37) \times 10^{28}\,\text{erg\,s}^{-1}\,M_\odot^{-1}$, $\beta = (1.62 \pm 0.22) \times 10^{39}\,\text{erg\,s}^{-1}\,M_\odot^{-1}\,\text{yr}$. To compare our sample with this relation of Lehmer et al. (2010) we made use of the equation 2.4 again to extrapolate our luminosities into the 2-10 keV energy band for which the relation was determined.

Following the analysis by Basu-Zych et al. (2013b), we plotted $\log_{10}(L_X/\text{SFR})$ vs. log(sSFR) for our studied galaxy sample, as can be seen in Figure 2.3. We have also plotted the Lehmer et al. (2010) relation shown as the green line, and it is evident the data of our studied sample are distinguishably above the Lehmer et al. (2010) relation for star-forming galaxies. Both from the plot and the equation
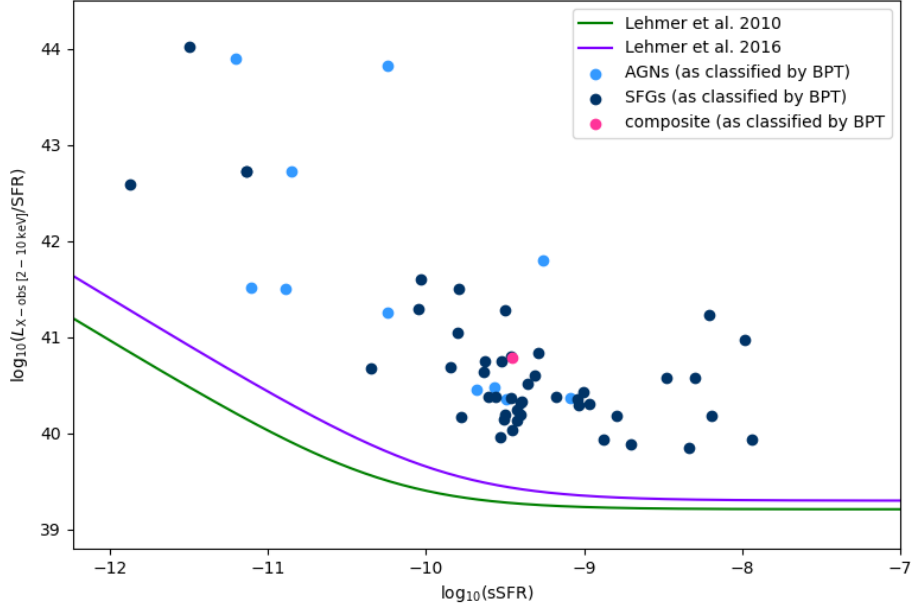
Figure 2.3: Studied dwarf galaxy sample in the diagram of X-ray luminosity over the SFR as dependent on the sSFR. Light blue points correspond to the galaxies determined to be AGNs according to the BPT diagnostics, dark blue are the galaxies classified as star-forming and pink points is the composite galaxy. The relation by Lehmer et al. (2010) is shown as the green line in the plot and the relation by Lehmer et al. (2016) as the purple line (where $< z >= 0.03$ was used). The observed 2-10 keV X-ray luminosity is in units of erg s^{-1}, the SFR is in units of $M_\odot$ yr^{-1} and the sSFR is the units of yr^{-1}.

2.5 it is visible that the (L_X/SFR) ratio should be constant for the galaxies dominated by HMXBs, which are the galaxies with sSFRs bigger than $\sim 10^{-10}$ (Lehmer et al., 2010). We have also plotted the Lehmer et al. (2016) relation (see equation 1.5) to show that our sample is still significantly above the line, even if redshift is considered (we considered redshift $< z >= 0.03$).

In Figure 2.3 we plotted our sample in three colours denoting their classification by the BPT diagnostic, where light blue points correspond to galaxies classified as AGNs, dark blue points to star-forming galaxies and pink points to composites, to see if there is any trend. We find, that there is no particular trend present (see 2.3).

In Figure 2.4 we plotted our sample galaxies by colours showing the fraction of their optical AGN luminosity compared with the one from the star-formation as determined by Birchall et al. (2020). We have chosen different categories of sizes of luminosities to those presented by Birchall et al. (2020) and added a category
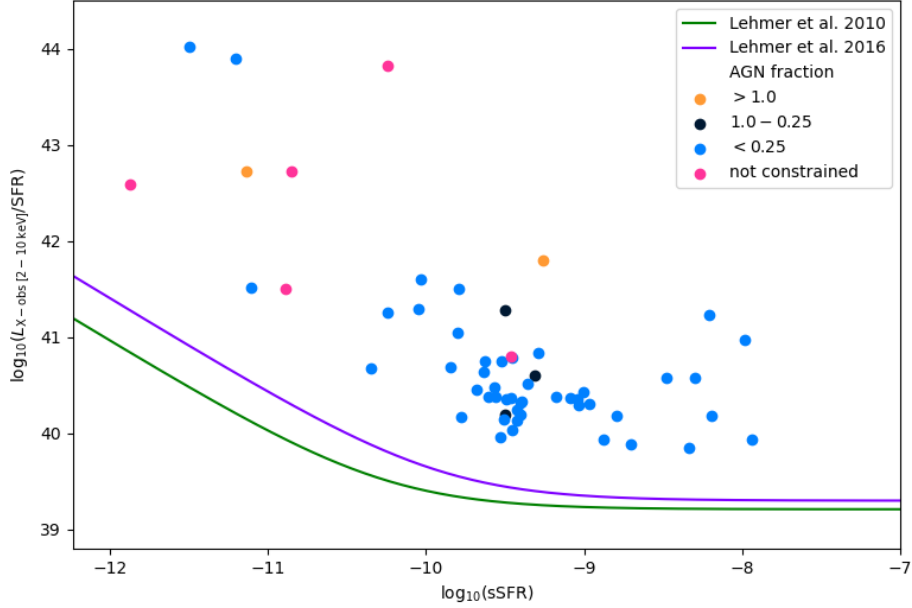
Figure 2.4: Our dwarf galaxy sample in the diagram of X-ray luminosity over the SFR as dependent on the sSFR. The galaxies are categorised by the fraction of their optical AGN luminosity compared with the one from the galaxy (Birchall et al., 2020). The relation by Lehmer et al. (2010) is shown as the green line in the plot and the relation by Lehmer et al. (2016) as the purple line (where $<z> = 0.03$ was used). The observed 2-10 keV X-ray luminosity is in units of erg s^{-1}, the SFR is in units of $M_\odot$ yr^{-1} and the sSFR is the units of yr^{-1}.

for those with not enough significant emission line flux detection (Line Flux/Line Flux Error >3), which in result were not studied for their optical properties by Birchall et al. (2020).

As we focus on the metallicity dependence of the X-ray luminosities, we have followed the analysis by Svoboda et al. (2019), in which they modified the L_{X}/SFR vs. sSFR plot for metallicity, according to the results of previous work by Brorby et al. (2016). The modification consists in applying a multiplicative factor $\left(\frac{(\mathrm{O/H})}{(\mathrm{O/H})_\odot}\right)^{0.59}$ to the (L_X/SFR) ratio for X-ray luminosities in the 0.5-8 keV energy band. This plot is shown in Figure 2.5. On this diagram, we have also plotted the Brorby et al. (2016) relation, shown as the blue line, which is only valid for HMXB dominated galaxies, and the galaxy samples of Mineo et al. (2012a); Brorby et al. (2016); Brorby and Kaaret (2017) and Svoboda et al. (2019). It is evident that again most of our sample is well above the line by Brorby et al. (2016). This shows that the relation by Brorby et al. (2016) does not work well for our sample, due to an excess in the X-ray luminosity.
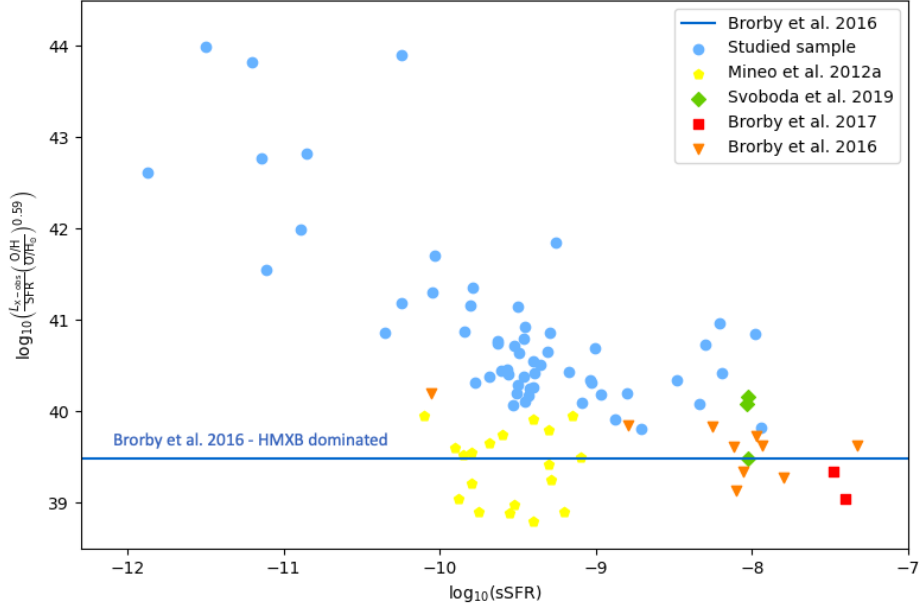
Figure 2.5: Our dwarf galaxy sample in the diagram of X-ray luminosity over the SFR scaled by a factor covering the metallicity dependence (according to results from Svoboda et al., 2019; Brorby et al., 2016) as a function of the sSFR. The yellow pentagons correspond to the star-forming galaxies from the Mineo et al. (2012a) sample. The green diamonds are the GPs from Svoboda et al. (2019). The red squares are the Green Pea analogues by Brorby and Kaaret (2017) and the orange triangles are the LBAs studied by Brorby et al. (2016). The relation by Brorby et al. (2016) is shown as the blue line in the plot. The observed 0.5-8 keV X-ray luminosity is in units of erg s^{-1}, the SFR is in units of $M_\odot$ yr^{-1} and the sSFR is the units of yr^{-1}.

2.4 Robustness of the observed X-ray luminosity excess across different methods

The relations by Mineo et al. (2012b) and Lehmer et al. (2016), equations 1.3 and 1.5, were used by Birchall et al. (2020) to calculate the predicted X-ray luminosity $L_X = L_{XRB} + L_{gas}$ for the studied sample. With our metallicity estimates, we have also used the relation by Brorby et al. (2016), equation 1.6, and also the relation by Mineo et al. (2014), equation 1.4, considering only the L_X-SFR plane. For all of these estimations we have used the extrapolation to the 2 - 12 keV energy band by equation 2.4, except the method used originally by Birchall et al. (2020), since the X-ray luminosity of hot gas (L_{gas} does not contribute significantly to the predicted X-ray luminosity and cannot be described by the power law with $\Gamma = 1.9$, we have therefore adopted their values for the X-ray luminosity (See

the prediction Le16, Mi12b in Table 2.3). We calculated the X-ray luminosity excess over the predicted value from all three methods of estimating the predicted emission. The X-ray excess, $L_{\mathrm{X-excess}}$, is determined as the difference between the observed and the predicted X-ray luminosity. Our results are summarised in Table 2.3).

It can be seen (see Table 2.3) that the predicted X-ray luminosities differ only slightly across the three methods, with a few being different by an order of magnitude. The J0123-0029 source differs by two orders of magnitude in the X-ray luminosity, with the method used by Birchall et al. (2020) yielding significantly larger luminosity than with the remaining two methods used. It is apparent, that this larger difference in predicted X-ray luminosities does not influence the X-ray excess considerably, since the excess is an another magnitude larger. Sources, which are significantly different (at least close to one magnitude difference) include: NGC 4117, LEDA 39539, NGC 4395, LEDA 44693 and J0304-0112. Again, their differences in the predicted X-ray luminosities from XRBs does not show up in the X-ray excess estimations - the X-ray luminosities are almost always at least an order of magnitude smaller than the X-ray excess values. Hence, for a given galaxy, the X-ray excess is practically the same across all methods adopted. So we can say that the metallicity dependence used by Brorby et al. (2016) is rather a correction of the predicted value, as was already discussed in Section 2.3. Galaxies NGC 4395, J0114+0013, J0304-0112, J2205-0030 and J2347+0103 show a significant X-ray excess between 3 to 5 orders of magnitude higher than the predicted luminosity. In contrast, sources LEDA 30866 and J1213+1413 show excess only slightly more than three times larger than the predicted value.

Abbr. Name	L_{X-obs} (erg s^{-1})			Mineo2014 L_{X-pred} (erg s^{-1})	Brorby2016 L_{X-pred} (erg s^{-1})	Le16,Mi12b L_{X-pred} (erg s^{-1})	Mineo2014 $L_{X-excess}$ (erg s^{-1})	Brorby2016 $L_{X-excess}$ (erg s^{-1})	Le16,Mi12b $L_{X-excess}$ (erg s^{-1})
J0115+0038	4.90E+40	±	5.1E40	3.92E+38	6.67E+38	5.47E+38	4.86E+40	4.83E+40	4.85E+40
J0145+0010	7.77E+40	±	6.4E40	1.02E+39	1.71E+39	1.21E+39	7.67E+40	7.60E+40	7.65E+40
J0241-0013	4.71E+39	±	7.7E39	8.04E+38	6.99E+38	1.1E+39	3.91E+39	4.01E+39	3.61E+39
J0256+0603	3.41E+39	±	1.9E40	9.06E+37	1.50E+38	7.62E+37	3.32E+39	3.26E+39	3.33E+39
LEDA 2402319	3.19E+40	±	4.1E40	1.85E+39	1.68E+39	2.28E+39	3.00E+40	3.02E+40	2.96E+40
J0819+2103	2.69E+39	±	4.8E39	1.41E+38	1.14E+38	3.86E+38	2.55E+39	2.58E+39	2.30E+39
J0822+0345	1.13E+40	±	4.9E39	3.67E+39	5.37E+39	3.24E+39	7.63E+39	5.93E+39	8.06E+39
J0832+1912	4.16E+40	±	1.8E40	4.54E+39	1.03E+40	4.32E+39	3.71E+40	3.13E+40	3.73E+40
J0856+3804	7.70E+39	±	1.4E40	8.04E+38	9.38E+38	9.42E+38	6.90E+39	6.76E+39	6.76E+39
J0903+1511	1.46E+40	±	9.8E39	1.89E+38	2.20E+38	3.44E+38	1.44E+40	1.44E+40	1.43E+40
SDSSCGB 15.2	4.24E+40	±	2.9E40	7.05E+39	8.20E+39	6.33E+39	3.53E+40	3.42E+40	3.61E+40
J0927+3624	7.88E+39	±	3.7E39	3.19E+38	3.91E+38	3.44E+38	7.56E+39	7.49E+39	7.54E+39
J1008+1256	1.93E+40	±	1.3E40	9.96E+38	7.98E+38	1.45E+39	1.83E+40	1.85E+40	1.79E+40
J1025+1245	8.44E+39	±	1.7E40	9.26E+38	5.97E+38	1.03E+39	7.51E+39	7.84E+39	7.41E+39
LEDA 30866	3.12E+39	±	2.4E40	1.10E+39	8.01E+38	9.49E+38	2.02E+39	2.32E+39	2.17E+39
Mrk 1434	1.18E+40	±	3.0E39	1.74E+38	3.90E+38	1.44E+38	1.16E+40	1.14E+40	1.17E+40
J1038+5330	3.78E+39	±	2.4E38	6.18E+38	-	5.1E+38	3.16E+39	-	3.27E+39
LEDA 2116718	3.11E+39	±	2.3E40	4.43E+38	5.42E+38	4.73E+38	2.67E+39	2.57E+39	2.64E+39
UGC 6192	1.60E+39	±	4.2E38	1.42E+38	2.06E+38	1.74E+38	1.46E+39	1.39E+39	1.43E+39
J1128+5330	4.01E+40	±	5.5E39	1.66E+39	1.47E+39	1.76E+39	3.84E+40	3.86E+40	3.83E+40
J1129+5823	2.99E+40	±	3.4E40	3.30E+39	4.23E+39	3.12E+39	2.66E+40	2.57E+40	2.68E+40
Mrk 1303	1.06E+40	±	6.7E39	3.10E+39	3.97E+39	2.79E+39	7.50E+39	6.63E+39	7.81E+39
J1145+1945	1.02E+40	±	7.2E39	2.43E+38	-	7.65E+38	9.96E+39	-	9.44E+39
J1155+2327	3.80E+40	±	2.1E40	4.04E+39	4.26E+39	4.02E+39	3.40E+40	3.37E+40	3.40E+40
NGC 4117	6.17E+39	±	5.0E38	4.80E+37	5.39E+37	5.53E+38	6.12E+39	6.12E+39	5.62E+39
ECO 11516	2.21E+40	±	1.3E40	3.10E+38	4.37E+38	7.31E+38	2.18E+40	2.17E+40	2.14E+40
J1213+1413	3.36E+39	±	8.5E39	9.26E+38	8.85E+38	1.05E+39	2.43E+39	2.47E+39	2.31E+39
J1217+0340	2.24E+39	±	1.4E39	1.50E+38	1.30E+38	1.25E+38	2.09E+39	2.11E+39	2.12E+39
LEDA 39539	2.47E+39	±	1.3E39	5.36E+36	-	5.62E+37	2.46E+39	-	2.41E+39
NGC 4395	1.39E+40	±	7.0E38	4.43E+35	6.53E+35	6.23E+36	1.39E+40	1.39E+40	1.39E+40
J1235+3931	1.10E+40	±	4.4E39	7.34E+38	8.51E+38	6.26E+38	1.03E+40	9.48E+39	1.04E+40
J1235-0012	7.14E+39	±	9.3E39	1.17E+39	8.41E+38	9.89E+38	5.97E+39	6.30E+39	6.15E+39
LEDA 44693	8.02E+39	±	6.0E39	6.26E+37	2.51E+37	4.77E+38	7.96E+39	7.99E+39	7.54E+39
1258+27W06	2.45E+40	±	2.3E40	2.93E+39	2.14E+39	3.1E+39	2.16E+40	2.24E+40	2.14E+40
J1307+5357	4.89E+40	±	3.3E40	6.21E+39	7.32E+39	5.78E+39	4.27E+40	4.16E+40	4.31E+40
J1308+1130	4.99E+39	±	1.5E40	6.12E+38	1.01E+39	5.6E+38	4.38E+39	3.98E+39	4.43E+39
J1319+5521	7.34E+39	±	6.0E39	7.68E+38	8.07E+38	9.04E+38	6.57E+39	6.53E+39	6.44E+39
J1341+2630	5.54E+40	±	1.2E41	3.44E+39	3.79E+39	3.67E+39	5.20E+40	5.16E+40	5.17E+40
J1344+5601	1.57E+41	±	8.2E40	4.52E+40	7.30E+40	3.99E+40	1.12E+41	8.40E+40	1.17E+41
J1347+5814	1.23E+40	±	5.5E39	1.43E+39	1.45E+39	1.52E+39	1.09E+40	1.08E+40	1.08E+40
J1347+1734	8.88E+41	±	5.9E40	3.56E+39	3.88E+39	3.59E+39	8.84E+41	8.84E+41	8.84E+41
UGC 9215	3.85E+39	±	1.6E39	6.12E+38	6.02E+38	6.61E+38	3.24E+39	3.25E+39	3.19E+39
J1431+2816	8.26E+39	±	9.3E39	8.86E+38	1.05E+39	9.71E+38	7.37E+39	7.21E+39	7.29E+39
J1440+0247	2.42E+40	±	8.1E39	2.03E+39	2.58E+39	2.36E+39	2.22E+40	2.16E+40	2.18E+40
J1440+0331	4.34E+39	±	8.9E39	4.01E+38	2.73E+38	3.74E+38	3.94E+39	4.07E+39	3.97E+39
ECO 2050	2.07E+39	±	4.8E39	3.75E+38	4.03E+38	4.17E+38	1.69E+39	1.67E+39	1.65E+39
J1537+5515	1.13E+39	±	1.8E38	6.94E+37	-	5.82E+37	1.06E+39	-	1.07E+39
J1548+3507	7.10E+39	±	1.4E40	1.64E+39	1.72E+39	1.85E+39	5.46E+39	5.38E+39	5.25E+39
J1605+1748	6.91E+40	±	3.2E40	4.32E+38	4.19E+38	7.73E+38	6.87E+40	6.87E+40	6.83E+40
AGC 262533	3.16E+39	±	9.4E38	1.39E+38	1.85E+38	1.53E+38	3.02E+39	2.98E+39	3.01E+39
J1613+5105	1.09E+40	±	2.0E40	1.76E+39	1.82E+39	1.88E+39	9.14E+39	9.08E+39	9.02E+39
J1626+3908	3.04E+40	±	1.4E40	1.10E+39	1.27E+39	1.11E+39	2.93E+40	2.91E+40	2.93E+40
J1627+3854	1.60E+40	±	1.8E40	7.14E+38	8.85E+38	8.69E+38	1.53E+40	1.51E+40	1.51E+40
J2137+0028	3.95E+39	±	8.9E39	7.22E+38	8.17E+38	7.97E+38	3.23E+39	3.13E+39	3.15E+39
J2137+0031	2.34E+40	±	2.2E40	5.28E+38	4.95E+38	7.63E+38	2.29E+40	2.27E+40	2.26E+40
gJ2332-0050	1.35E+40	±	9.8E39	1.03E+39	1.27E+39	1.05E+39	1.25E+40	1.26E+40	1.25E+40
J0114+0013	1.59E+41	±	6.2E41	7.65E+37	1.72E+37	6.63E+38	1.59E+41	1.59E+41	1.58E+41
J0123-0029	5.02E+39	±	1.3E40	3.22E+36	3.73E+36	2.15E+38	5.02E+39	4.85E+39	4.81E+39
J0304-0112	5.66E+40	±	2.6E40	1.37E+36	1.75E+36	3.81E+37	5.66E+40	5.65E+40	5.66E+40
J2205-0030	1.27E+41	±	8.6E40	5.95E+37	6.67E+37	8.64E+38	1.27E+41	1.27E+41	1.26E+41
J2347+0103	5.35E+42	±	5.2E42	2.04E+38	2.06E+38	7.09E+38	5.35E+42	5.35E+42	5.35E+42

Table 2.3: Observed 2 - 12 keV X-ray luminosity by Birchall et al. (2020). Estimations of the predicted X-ray luminosities in the 2 - 12 keV band, using relations by Mineo et al. (2012b, 2014); Lehmer et al. (2016); Brorby et al. (2016) and their luminosity excesses. The values of Le16, Mi12b luminosty predictions adopted from Birchall et al. (2020).

3. Discussion

In this Section, we discuss the effects of metallicity on the X-ray luminosity, including a discussion of considerably different metallicity values. Then, we discuss possible explanations of the enhanced X-ray luminosity, including AGNs, other possible sources and statistical effects. And last, we consider the implications on AGN classification methods.

3.1   Effects of metallicity

Metallicity has influence on X-ray luminosity according to various studies (e.g., Douna et al., 2015; Brorby et al., 2016; Fornasini et al., 2020), but in the sample of Birchall et al. (2020), the typical metallicities are not so largely different from solar values. With the mean value, using the Pettini and Pagel (2004) method for galaxy metallicity estimation, being slightly sub-solar $12 + \log(\mathrm{O/H}) = 8.42$. This was well demonstrated by the relatively minor shifts in the diagram plotting the L_{X}-SFR-metallicity plane (see Figure 2.1).

The enhanced X-ray luminosity flux cannot be explained by metallicity, as it is evident from our results that it does not influence the X-ray luminosity substantially enough. This was well illustrated by our comparison of observed X-ray luminosity with different predictions and their respective excess X-ray luminosities (see Section 2.4, more specifically Table 2.3). It is evident that the excess X-ray luminosity does not significantly depend on the method chosen for the predictions. Even the most simple relation (out of the three used) with no metallicity considered by Mineo et al. (2014) shows essentially the same excess luminosities as the two other more detailed methods applied. In the Brorby et al. (2016) relation, metallicity is considered directly. Contrarily, in the luminosity prediction used by Birchall et al. (2020) (based on Mineo et al., 2012b; Lehmer et al., 2016) metallicity is not directly taken into account. As was discussed in Section 1.2.4, metallicity is correlated with stellar mass (Tremonti et al., 2004; Baldry et al., 2008), and in consequence the prediction of Birchall et al. (2020) (using the Lehmer et al., 2016 relation, see equation 1.5) is also indirectly dependent on metallicity.

Since the Lehmer et al. (2016) relation indirectly depends on metallicity, we

Abbr. Name	$\log M_*$ $(M_\odot)$	$\log M_{*,\mathrm{met}}$ $(M_\odot)$	Lehmer16 $L_{\mathrm{X-pred}}$ (erg s^{-1})	Le16, Tr04 $L_{\mathrm{X-pred}}$ (erg s^{-1})	Brorby16 $L_{\mathrm{X-pred}}$ (erg s^{-1})	Lehmer16 $L_{\mathrm{X-excess}}$ (erg s^{-1})	Le16, Tr04 $L_{\mathrm{X-excess}}$ (erg s^{-1})	Brorby16 $L_{\mathrm{X-excess}}$ (erg s^{-1})
J0115+0038	8.93	8.45	5.16E+38	3.92E+38	6.67E+38	4.85E+40	4.86E+40	4.83E+40
J0145+0010	9.06	8.46	1.13E+39	9.45E+38	1.71E+39	7.66E+40	7.68E+40	7.60E+40
J0241-0013	9.23	9.00	1.04E+39	9.17E+38	6.99E+38	3.67E+39	3.79E+39	4.01E+39
J0256+0603	6.49	8.47	6.94E+37	1.54E+38	1.50E+38	3.34E+39	3.26E+39	3.26E+39
LEDA 2402319	9.45	8.97	2.14E+39	1.74E+39	1.68E+39	2.98E+40	3.02E+40	3.02E+40
J0819+2103	9.05	9.06	3.75E+38	4.21E+38	1.14E+38	2.31E+39	2.27E+39	2.58E+39
J0822+0345	8.82	8.58	2.97E+38	3.02E+39	5.37E+39	8.33E+39	8.28E+39	5.93E+39
J0832+1912	9.29	8.22	3.98E+39	3.66E+39	1.03E+40	3.76E+40	3.79E+40	3.13E+40
J0856+3804	9.02	8.76	8.83E+38	8.08E+38	9.38E+38	6.82E+39	6.89E+39	6.76E+39
J0903+1511	8.87	8.76	3.30E+38	3.11E+38	2.20E+38	1.43E+40	1.43E+40	1.44E+40
SDSSCGB 15.2	9.20	8.77	5.78E+39	5.76E+39	8.20E+39	3.66E+40	3.66E+40	3.42E+40
J0927+3624	8.52	8.72	3.20E+38	3.92E+38	3.91E+38	7.56E+39	7.49E+39	7.49E+39
J1008+1256	9.39	9.07	1.37E+39	1.12E+39	7.98E+38	1.79E+40	1.82E+40	1.85E+40
J1025+1245	9.01	9.25	9.59E+38	1.23E+39	5.97E+38	7.48E+39	7.21E+39	7.84E+39
LEDA 30866	7.92	9.15	8.65E+38	1.28E+39	8.01E+38	2.25E+39	1.84E+39	2.32E+39
Mrk 1434	7.00	8.23	1.31E+38	1.78E+38	3.90E+38	1.17E+40	1.16E+40	1.14E+40
LEDA 2116718	8.62	8.72	4.40E+38	4.97E+38	5.42E+38	2.67E+39	2.61E+39	2.57E+39
UGC 6192	8.39	8.59	1.63E+38	2.12E+38	2.06E+38	1.44E+39	1.39E+39	1.39E+39
J1128+5330	9.22	8.99	1.63E+39	1.53E+39	1.47E+39	3.85E+40	3.86E+40	3.86E+40
J1129+5823	9.11	8.69	2.87E+39	2.78E+39	4.23E+39	2.70E+40	2.71E+40	2.57E+40
Mrk 1303	8.92	8.69	2.54E+39	2.56E+39	3.97E+39	8.06E+39	8.04E+39	6.63E+39
J1155+2327	9.33	8.84	3.71E+39	3.48E+39	4.26E+39	3.43E+40	3.45E+40	3.37E+40
NGC 4117	9.34	8.79	5.50E+38	2.02E+38	5.39E+37	5.62E+39	5.97E+39	6.12E+39
ECO 11516	9.28	8.61	7.06E+38	3.55E+38	4.37E+38	2.14E+40	2.17E+40	2.17E+40
J1213+1413	9.05	8.93	9.73E+38	9.58E+38	8.85E+38	2.39E+39	2.40E+39	2.47E+39
J1217+0340	7.02	9.01	1.13E+38	3.85E+38	1.30E+38	2.13E+39	1.85E+39	2.11E+39
NGC 4395	7.40	8.57	6.20E+36	9.89E+37	6.53E+35	1.39E+40	1.38E+40	1.39E+40
J1235+3931	7.89	8.29	5.71E+38	6.26E+38	1.52E+39	1.04E+40	1.04E+40	9.48E+39
J1235-0012	7.81	9.16	9.00E+38	1.32E+39	8.41E+38	6.24E+39	5.82E+39	6.30E+39
LEDA 44693	9.24	9.64	4.72E+38	1.25E+39	2.51E+37	7.55E+39	6.77E+39	7.99E+39
1258+27W06	9.42	9.15	2.87E+39	2.69E+39	2.14E+39	2.16E+40	2.18E+40	2.24E+40
J1307+5357	9.37	8.75	5.31E+39	5.05E+39	7.32E+39	4.36E+40	4.38E+40	4.16E+40
J1308+1130	8.31	8.48	5.13E+38	5.64E+38	1.01E+39	4.48E+39	4.43E+39	3.98E+39
J1319+5521	9.04	8.85	8.47E+38	7.95E+38	8.07E+38	6.49E+39	6.54E+39	6.53E+39
J1341+2630	9.40	8.81	3.42E+39	3.05E+39	3.79E+39	5.20E+40	5.23E+40	5.16E+40
J1344+5601	9.15	8.50	3.64E+40	3.76E+40	7.30E+40	1.21E+41	1.19E+41	8.40E+40
J1347+5814	9.10	8.88	1.41E+39	1.35E+39	1.45E+39	1.09E+40	1.09E+40	1.08E+40
J1347+1734	9.36	8.82	3.34E+39	3.05E+39	3.88E+39	8.85E+41	8.85E+41	8.84E+41
UGC 9215	8.84	8.90	6.15E+38	6.80E+38	6.02E+38	3.24E+39	3.17E+39	3.25E+39
J1431+2816	8.96	8.75	9.05E+38	8.58E+38	1.05E+39	7.36E+39	7.40E+39	7.21E+39
J1440+0247	9.42	8.69	2.21E+39	1.74E+39	2.58E+39	2.20E+40	2.25E+40	2.16E+40
J1440+0331	8.16	9.20	3.42E+38	7.66E+38	2.73E+38	4.00E+39	3.57E+39	4.07E+39
ECO 2050	8.63	8.83	3.88E+38	4.80E+38	4.03E+38	1.68E+39	1.59E+39	1.67E+39
J1548+3507	9.22	8.85	1.72E+39	1.55E+39	1.72E+39	5.38E+39	5.55E+39	5.38E+39
J1605+1748	9.21	8.91	7.39E+38	5.72E+38	4.19E+38	6.84E+40	6.85E+40	6.87E+40
AGC 262533	8.21	8.66	1.43E+38	2.29E+38	1.85E+38	3.02E+39	2.93E+39	2.98E+39
J1613+5105	9.20	8.87	1.74E+39	1.60E+39	1.82E+39	9.16E+39	9.30E+39	9.08E+39
J1626+3908	8.88	8.77	1.03E+39	1.03E+39	1.27E+39	2.94E+40	2.94E+40	2.91E+40
J1627+3854	9.03	8.71	8.15E+38	7.10E+38	8.85E+38	1.52E+40	1.53E+40	1.51E+40
J2137+0028	8.84	8.79	7.43E+38	7.66E+38	8.17E+38	3.21E+39	3.18E+39	3.13E+39
J2137+0031	9.08	8.94	7.21E+38	6.83E+38	4.95E+38	2.27E+40	2.27E+40	2.29E+40
gJ2332-0050	8.92	8.72	9.73E+38	9.42E+38	1.27E+39	1.25E+40	1.26E+40	1.22E+40
J0114+0013	9.28	8.93	6.44E+38	3.57E+38	7.26E+37	1.58E+41	1.59E+41	1.59E+41
J0123-0029	8.93	8.77	2.14E+38	1.66E+38	3.73E+36	4.81E+39	4.85E+39	5.02E+39
J0304-0112	8.18	8.69	3.77E+37	1.33E+38	1.75E+36	5.66E+40	5.65E+40	5.66E+40
J2205-0030	9.47	8.80	8.52E+38	2.43E+38	6.67E+37	1.26E+41	1.27E+41	1.27E+41
J2347+0103	9.10	8.88	6.62E+38	5.21E+38	2.06E+38	5.35E+42	5.35E+42	5.35E+42

Table 3.1: Stellar masses M_* from the MPA-JHU catalogue as a comparison to calculated stellar masses $M_{*,\mathrm{met}}$ from the Tremonti et al. (2004) mass-metallicity relation. The estimations of mass from metallicity were done for our 57 galaxy sub-sample with previously estimated metallicities by the PE04 method. Estimations of the predicted X-ray luminosities in the 2 - 12 keV band, using relation by Lehmer et al. (2016) and their respective luminosity excesses.

calculated the stellar mass estimations using the mass-metallicity relation as derived in (Tremonti et al., 2004) (see equation 1.2). We have used our metallicity estimations (see section 2.2) in our calculations, and so it has been done only for our sub-sample containing 57 galaxies with metallicity values. We have also determined the predicted X-ray luminosity in the 2-12 keV band, using the Lehmer et al. (2016) relation both with the stellar masses from the MPA-JHU and the stellar mass calculations from metallicities using the mass-metallicity relation by Tremonti et al. (2004), and their respective X-ray excess luminosities. We have also compared these values with the previously (see Section 2.4) determined X-ray predictions from Brorby et al. (2016), where the dependence on metallicity is stronger, since it is direct.

It can be seen (see Table 3.1), that the stellar masses calculated from metallicities are close to the values from the MPA-JHU catalogue. Similarly both relations using the Lehmer et al. (2016) give similar results. In comparison with the Brorby et al. (2016) relation, both the Lehmer et al. (2016) relations also give similar results, although it is apparent there are more differences in some sources. We also must point out, that the mass-metallicity relation by Tremonti et al. (2004) is valid for the stellar mass range of $8.5 < M_* < 11.5$ and not all of our sources satisfy this constraint, according to the MPA-JHU catalogue (e.g., J0256+0603, LEDA 30866). For these sources, it is also apparent the relation by Tremonti et al. (2004) overestimates the values.

If the metallicities were more on the extreme end of the metallicity spectrum, the shifts in the L_X-SFR-metallicity plane would be slightly more significant. For some of the most metal-poor blue compact dwarf starburst galaxies I Zw 18 and SBS 0335-052 studied by e.g., Kunth and Östlin (2000), the metallicities reach as low as $12 + \log(\mathrm{O/H}) = 7.2$ (Izotov et al., 1999). Recently Izotov et al. (2018) discovered that a star-forming galaxy J0811+4730 has extremely low metallicity $12 + \log(\mathrm{O/H}) = 6.98$. Some of the more common dwarf starburst galaxy metallicities are ~ 8, as an example II Zw 40 with $12 + \log(\mathrm{O/H}) = 8.09$ (Guseva et al., 2000), which is closer in metallicity to our studied galaxy sample. It is important to note, that some galaxies of our studied sample had very low metallicities reaching as low as $12 + \log(\mathrm{O/H}) = 7.90$, but even for these galaxies the excess in X-ray luminosity could not have been explained by adding the L_x/SFR and metallicity relation. We therefore concluded, that metallicity is a

correction rather than being an explanation for the differences in observed and predicted luminosities. If the X-ray luminosity prediction by Brorby et al. (2016), where metallicity is directly taken into account, is used, the excess for three galaxies (J0822+0345, Mrk 1303 and J1344+5601) will not be significant enough to satisfy the X-ray excess criterion by Birchall et al. (2020) ($L_{\mathrm{X-obs}}/L_{\mathrm{pred}} > 3$) and they would have been excluded from their original sample. In all three cases, the ratio of observed to predicted luminosity would be closer to 2, hence even if metallicity is a correction, it does influence the X-ray luminosity and its excess, especially for sources where the ratio was low in the first place (all three galaxies had the ratio close to 4). For the two sources with the ratio close to 3, mentioned in 2.4, however, the employment of the Brorby et al. (2016) method would not exclude them from the original sample.

We have estimated metallicities of the sample of Birchall et al. (2020) by three methods, compared them with the values taken from the MPA-JHU catalogue and decided to use the method by Pettini and Pagel (2004) for our estimations (see Section 2.2). It should be pointed out that the estimations vary rather considerably between methodologies, with the largest difference in mean values being between the methods by Pilyugin and Mattsson (2011) and Tremonti et al. (2004) (the analytical estimate), mean values 8.30 and 8.80 respectively. This evidently could slightly influence our results, since as was discussed previously, we have used the method, which yielded slightly sub-solar mean metallicity, for our further estimations. With sub-solar metallicities the shift on the L_{X}-SFR-metallicity plane is to the right, which means closer to the relation of Brorby et al. (2016) (see Figures 2.1 and 2.2). Conversely, if the metallicities were higher than solar for most galaxies, the shift would be mostly to the left on the diagram and the predicted luminosities would be even further from the Brorby et al. (2016) relation for star-forming galaxies. Furthermore, the mean metallicity for values taken from the MPA-JHU catalogue is 8.63, which is almost identical to solar, and the differences would be even less prominent.

3.2 Explanation of enhanced L_X

3.2.1 AGNs in dwarf galaxies?

Based on the observed X-ray excess, Birchall et al. (2020) identified 61 possible AGN hosts from the parent sample of ~ 4000 dwarf galaxies. 85% of these AGN candidates were not identified by optical AGN diagnostics (implications of which will be discussed in Section 3.3). They have also concluded, consistently with other studies by e.g., Georgakakis et al. (2017), that low luminosity AGNs can be expected to be more common in dwarfs galaxies than can be detected now.

As was noted previously, we concluded the excess in X-ray luminosities cannot be explained by metallicity. Hence, in accordance with the research of Birchall et al. (2020), AGNs can indeed be considered as possible sources of X-ray excess luminosity in our studied dwarf galaxy sample.

3.2.2 Other possible sources?

The X-ray excess luminosities are mostly in the orders of 10^{39} or 10^{40} erg s^{-1} with only 4 having an excess flux of order 10^{41} erg s^{-1} and only 1 of order 10^{42} erg s^{-1} (see Table 2.3). Therefore, there is a possibility that some of the galaxies in the studied sample can have enhanced luminosity caused by some other source rather than an AGN.

One possible explanation could be an enhanced HMXB population, as studied by Brorby et al. (2014) for very low metallicity BCDs. The metallicities in our studied sample are significantly higher than those of Brorby et al. (2014), as they only studied galaxies such as that $12 + \log(\mathrm{O/H}) < 7.7$ and our sample is, on avarage, only slightly sub-solar, therefore it is not likely that there could be an enhanced HMXB population in our sample.

Another possible source could be an ULX, which generally have X-ray luminosity in the order of 10^{39} erg s^{-1} (e.g., Kaaret et al. 2017). Statistical correction on the sample was also performed by Birchall et al. (2020), in which they have also considered ULXs as possible sources. Their research showed that the probability of the sample having one ULX rather than an AGN is 76%, two ULXs then 36%. They also covered the possibility of having an enhanced HMXB population, deeming it plausible mostly for the lowest mass dwarfs in the sample and con-

cluded that in the higher mass dwarfs, the sources are most likely AGNs. This is consistent with the fact, that metallicity is generally smaller in lower mass galaxies (see mass-metallicity relation by e.g., Tremonti et al. 2004), and therefore can influence the X-ray emission more than in higher mass galaxies.

3.2.3   Statistical effects?

The sample of X-ray enhanced luminosities by Birchall et al. (2020) counts 61 sources out of ~3400. A legitimate question is, whether this small fraction represents a unique set of dwarf-galaxy sources with a different source of X-ray emission, or whether it represents a fraction of sources with the largest positive scatter of the X-ray luminosity. The stochasticity effect of the L_X-SFR relation was studied by Gilfanov et al. (2004) and Justham and Schawinski (2012). They have shown that, due to a substantial stochastic variation, a large spread of X-ray luminosities can be obtained for low luminosity and low SFR systems. Indeed, some sources in the studied sample have both quantities relatively low (see Table 2.1), and thus the proper estimate of the stochasticity effect would be beneficial before drawing conclusions about the AGN fractions in the total sample, however, this is beyond the scope of this thesis.

To determine the observed X-ray luminosities, Birchall et al. (2020) used the 3XMM catalogue by Rosen et al. (2016). Any survey is biased due to the methodology used or the limited sensitivity of the instruments. The X-ray luminosity measurements used by Birchall et al. (2020), and subsequently us, have relatively large errors (see Table 2.1), which we have not included in our diagrams for better clarity. Nevertheless, it must be noted some of the errors are in the same orders as the X-ray luminosities, with few having errors order of magnitude larger than the measured luminosity. For some galaxies in the sample, it is consistent with them possibly having zero flux. That would also mean that no excess luminosity is observed and that no other sources are present - including the considered AGNs and other sources.

Perhaps, a stronger criterion than the one proposed by Birchall et al. (2020), $L_\mathrm{X-obs}/L_\mathrm{X-pred} > 3$, could be used to further reduce the sample. For instance, if a criterion of $L_\mathrm{X-obs}/L_\mathrm{X-pred} > 10$ were used, 28 sources would be further excluded from the sample. Rather than introducing a stronger criterion, it may be beneficial to look at the absolute X-ray flux. If the X-ray excess is in the order

of $\approx 10^{42}$, AGN would be a very likely source, for it would be difficult to explain the flux otherwise (see e.g., Svoboda et al. 2019). On the other hand, some of the X-ray excess luminosities of our studied sample are smaller than 10^{40} (see Table 2.3), and they could therefore be explained by an ULX or an enhanced HMXB population, as we have already discussed.

3.3   Implication for AGN classification

If the conclusions by Birchall et al. (2020) about the AGN fraction are indeed correct, and 85% of those 61 galaxies identified as AGNs did not show up in the optical classification, it could have implication on the use of the optical classification as an only method of classifying AGNs. This would suggest that another method needs to be used along the optical classification by the BPT diagram, and in that respect X-ray measurements could be used as an additional method of AGN classification in dwarf galaxies. Especially for low luminosity AGNs, in which the star formation can obscure the weaker AGN activity, as has been demonstrated by Moran et al. (2002) for narrow line AGNs and by Cann et al. (2019) for star-forming galaxies.

There have been research conducted by Cid Fernandes et al. (2010) on the bias in the SDSS against weak line galaxies, which do not have strong enough emission line fluxes needed for the BPT diagnostic. They argue, that the requirement for all four emission lines, where signal to rate ratio $S/N \geq 3$, is too strict for weak line galaxies and thus the BPT classification is not always reliable for weaker AGNs. They have proposed an alternative diagnostic diagrams, which have been used in further studies concerning AGNs, one example being the study of Kristensen et al. (2020), who implemented the use of the classic BPT diagram along with the WHAM diagram of Cid Fernandes et al. (2010), (2011) for sample selection.

The classification of AGNs in the low-mass dwarf galaxies is susceptible to numerous errors, and they have to be approached in a different manner (Trump et al., 2015). There is no consensus regarding the different approaches to AGNs in dwarf galaxies, with various studies suggesting that a number of AGNs in dwarf galaxies will not be classified as such via the optical based diagnostics, despite showing AGN properties with other diagnostic measures (Cann et al., 2019), including X-ray based diagnostics. In contrast, studies by Trump et al. (2015);

Hainline et al. (2016) and most recently Dickey et al. (2019) show, that there is a high possibility of falsely identifying AGNs if the classification requirements become too lenient. If these false positives are then incorrectly included in AGN galaxy samples, it makes the samples skewed and the determined properties could be inaccurate for true AGN populations.

This could be a similar case with the research about star-forming galaxies (see e.g., Brorby et al., 2016; Lehmer et al., 2016), which could in turn include optically hidden low luminosity AGNs and the relations obtained could be less reliable. As numerous studies (e.g., Birchall et al., 2020; Mezcua and Domínguez Sánchez, 2020) identified possible obscured AGNs in dwarf galaxies, the X-ray luminosity relations, but not only, for star-forming galaxies need to be researched in detail with consideration of the possibility of previous inclusion of weak AGNs in the star-forming galaxy samples.

4. Conclusions

In this thesis, we have considered the effects of metallicity on the X-ray luminosity for the sample of dwarf galaxies that were proposed to host an AGN based on X-ray excess measurements by Birchall et al. (2020). Low metallicity leads to higher X-ray emission from star formation. Nevertheless, we found that the metallicity of the studied sources is on average sub-solar, but not largely different from the usual value of galaxies, for which the L_X-SFR relations were derived. Therefore, our re-calculation of the predicted X-ray luminosities provides only a relatively minor correction of the predicted values and our results are still in accordance with the original conclusions of Birchall et al. (2020), since metallicity cannot explain the enhanced X-ray luminosity of the studied sample. We have also found that the X-ray luminosity excess is not influenced considerably according to the method of prediction used (see Table 2.3).

We have plotted the studied sources in the L_X-SFR-metallicity planes and in diagrams using the sSFRs, rather than SFRs (see Section 2.3), and demonstrated that the sample shows an excess luminosity even if the relation with stellar mass is considered. We therefore confirm that the X-ray excess, as reported by Birchall et al. (2020), is found in this sample. Apart from their primary explanation by an AGN presence, we discuss other possibilities, including ultra-luminous X-ray sources. The possible presence of AGNs is also not universal for all sources in the sample, for some have considerable errors in their measured X-ray fluxes and would need to be more precisely studied. We have also compared our results with other studies of star-forming galaxies, some of which have also showed an X-ray excess flux and other sources, such as AGNs, were discussed.

The sources in our studied sample are interesting for further research, which could provide more insight into the Epoch of Reionisation. The majority of the galaxies are not classified as an AGN by the BPT diagnostics, nevertheless if their high X-ray emission is considered, the possibility of them being AGN hosts seems fairly plausible.

Bibliography

Anthony Aguirre, Lars Hernquist, Joop Schaye, David H. Weinberg, Neal Katz, and Jeffrey Gardner. Metal Enrichment of the Intergalactic Medium at z=3 by Galactic Winds. *The Astrophysical Journal*, 560(2):599–605, October 2001. doi: 10.1086/323070.

Anthony Aguirre, Corey Dow-Hygelund, Joop Schaye, and Tom Theuns. Metallicity of the Intergalactic Medium Using Pixel Statistics. IV. Oxygen. *The Astrophysical Journal*, 689(2):851–864, December 2008. doi: 10.1086/592554.

Carlos Allende Prieto, David L. Lambert, and Martin Asplund. The Forbidden Abundance of Oxygen in the Sun. *The Astrophysical Journal Letters*, 556(1): L63–L66, July 2001. doi: 10.1086/322874.

Peter Anninos. Computational Cosmology: From the Early Universe to the Large Scale Structure. *Living Reviews in Relativity*, 4(1):2, March 2001. doi: 10. 12942/lrr-2001-2.

I. K. Baldry, K. Glazebrook, and S. P. Driver. On the galaxy stellar mass function, the mass-metallicity relation and the implied baryonic mass function. *Monthly Notices of the Royal Astronomical Society*, 388(3):945–959, August 2008. doi: 10.1111/j.1365-2966.2008.13348.x.

J. A. Baldwin, M. M. Phillips, and R. Terlevich. Classification parameters for the emission-line spectra of extragalactic objects. *Publications of the Astronomical Society of the Pacific*, 93:5–19, February 1981. doi: 10.1086/130766.

R. Barkana and A. Loeb. In the beginning: the first sources of light and the reionization of the universe. *Physics Reports*, 349(2):125–238, July 2001. doi: 10.1016/S0370-1573(01)00019-9.

Antara R. Basu-Zych, Bret D. Lehmer, Ann E. Hornschemeier, Rychard J. Bouwens, Tassos Fragos, Pascal A. Oesch, Krzysztof Belczynski, W. N. Brandt, Vassiliki Kalogera, Bin Luo, Neal Miller, James R. Mullaney, Panayiotis Tzanavaris, Yongquan Xue, and Andreas Zezas. The X-Ray Star Formation Story as Told by Lyman Break Galaxies in the 4 Ms CDF-S. *The Astrophysical Journal*, 762(1):45, January 2013a. doi: 10.1088/0004-637X/762/1/45.

Antara R. Basu-Zych, Bret D. Lehmer, Ann E. Hornschemeier, Thiago S. Gonçalves, Tassos Fragos, Timothy M. Heckman, Roderik A. Overzier, Andrew F. Ptak, and David Schiminovich. Evidence for Elevated X-Ray Emission in Local Lyman Break Galaxy Analogs. *The Astrophysical Journal*, 774(2):152, September 2013b. doi: 10.1088/0004-637X/774/2/152.

Antara R. Basu-Zych, Bret Lehmer, Tassos Fragos, Ann Hornschemeier, Mihoko Yukita, Andreas Zezas, and Andy Ptak. Exploring the Overabundance of ULXs in Metal- and Dust-poor Local Lyman Break Analogs. *The Astrophysical Journal*, 818(2):140, February 2016. doi: 10.3847/0004-637X/818/2/140.

Serena Bertone, Gabriella De Lucia, and Peter A. Thomas. The recycling of gas and metals in galaxy formation: predictions of a dynamical feedback model. *Monthly Notices of the Royal Astronomical Society*, 379(3):1143–1154, August 2007. doi: 10.1111/j.1365-2966.2007.11997.x.

Keir L. Birchall, M. G. Watson, and J. Aird. X-ray detected AGN in SDSS dwarf galaxies. *Monthly Notices of the Royal Astronomical Society*, 492(2):2268–2284, February 2020. doi: 10.1093/mnras/staa040.

V. Bosch-Ramon. The role of AGN jets in the reionization epoch. *Astronomy & Astrophysics*, 617:L3, September 2018. doi: 10.1051/0004-6361/201833952.

J. Brinchmann, S. Charlot, S. D. M. White, C. Tremonti, G. Kauffmann, T. Heckman, and J. Brinkmann. The physical properties of star-forming galaxies in the low-redshift Universe. *Monthly Notices of the Royal Astronomical Society*, 351(4):1151–1179, July 2004. doi: 10.1111/j.1365-2966.2004.07881.x.

Jarle Brinchmann and Richard S. Ellis. The Mass Assembly and Star Formation Characteristics of Field Galaxies of Known Morphology. *The Astrophysical Journal Letters*, 536(2):L77–L80, June 2000. doi: 10.1086/312738.

Volker Bromm, Naoki Yoshida, Lars Hernquist, and Christopher F. McKee. The formation of the first stars and galaxies. *Nature*, 459(7243):49–54, May 2009. doi: 10.1038/nature07990.

M. Brorby and P. Kaaret. X-rays from Green Pea analogues. *Monthly Notices of the Royal Astronomical Society*, 470(1):606–611, May 2017. doi: 10.1093/mnras/stx1286.

M. Brorby, P. Kaaret, and A. Prestwich. X-ray binary formation in low-metallicity blue compact dwarf galaxies. *Monthly Notices of the Royal Astronomical Society*, 441(3):2346–2353, July 2014. doi: 10.1093/mnras/stu736.

M. Brorby, P. Kaaret, A. Prestwich, and I. F. Mirabel. Enhanced X-ray emission from Lyman break analogues and a possible L$_X$-SFR-metallicity plane. *Monthly Notices of the Royal Astronomical Society*, 457(4):4081–4088, April 2016. doi: 10.1093/mnras/stw284.

G. Bruzual and S. Charlot. Stellar population synthesis at the resolution of 2003. *Monthly Notices of the Royal Astronomical Society*, 344(4):1000–1028, October 2003. doi: 10.1046/j.1365-8711.2003.06897.x.

Jenna M. Cann, Shobita Satyapal, Nicholas P. Abel, Laura Blecha, Richard F. Mushotzky, Christopher S. Reynolds, and Nathan J. Secrest. The Limitations of Optical Spectroscopic Diagnostics in Identifying Active Galactic Nuclei in the Low-mass Regime. *The Astrophysical Journal Letters*, 870(1):L2, January 2019. doi: 10.3847/2041-8213/aaf88d.

Jenna M. Cann, Shobita Satyapal, Barry Rothberg, Gabriela Canalizo, Thomas Bohn, Stephanie LaMassa, William Matzko, Laura Blecha, Nathan J. Secrest, Anil Seth, Torsten Böker, Remington O. Sexton, Lara Kamal, and Henrique Schmitt. Relics of Supermassive Black Hole Seeds: The Discovery of an Accreting Black Hole in an Optically Normal, Low Metallicity Dwarf Galaxy. *arXiv e-prints*, art. arXiv:2104.05689, April 2021.

Carolin Cardamone, Kevin Schawinski, Marc Sarzi, Steven P. Bamford, Nicola Bennert, C. M. Urry, Chris Lintott, William C. Keel, John Parejko, Robert C. Nichol, Daniel Thomas, Dan Andreescu, Phil Murray, M. Jordan Raddick, Anže Slosar, Alex Szalay, and Jan Vandenberg. Galaxy Zoo Green Peas: discovery of a class of compact extremely star-forming galaxies. *Monthly Notices of the Royal Astronomical Society*, 399(3):1191–1205, November 2009. doi: 10.1111/j.1365-2966.2009.15383.x.

Hong-Yee Chiu. Gravitational Collapse. *Physics Today*, 17(5):21, January 1964. doi: 10.1063/1.3051610.

Tai L. Chow. *Gravity, Black Holes, and the Very Early Universe*. 2008. ISBN 978-0-387-73629-7. doi: 10.1007/978-0-387-73631-0.

R. Cid Fernandes, G. Stasińska, M. S. Schlickmann, A. Mateus, N. Vale Asari, W. Schoenell, and L. Sodré. Alternative diagnostic diagrams and the 'forgotten' population of weak line galaxies in the SDSS. *Monthly Notices of the Royal Astronomical Society*, 403(2):1036–1053, April 2010. doi: 10.1111/j.1365-2966. 2009.16185.x.

R. Cid Fernandes, G. Stasińska, A. Mateus, and N. Vale Asari. A comprehensive classification of galaxies in the Sloan Digital Sky Survey: how to tell true from fake AGN? *Monthly Notices of the Royal Astronomical Society*, 413(3):1687–1699, May 2011. doi: 10.1111/j.1365-2966.2011.18244.x.

Edward J. M. Colbert, Timothy M. Heckman, Andrew F. Ptak, David K. Strickland, and Kimberly A. Weaver. Old and Young X-Ray Point Source Populations in Nearby Galaxies. *The Astrophysical Journal*, 602(1):231–248, February 2004. doi: 10.1086/380899.

L. Cram, A. Hopkins, B. Mobasher, and M. Rowan-Robinson. Star Formation Rates in Faint Radio Galaxies. *The Astrophysical Journal*, 507(1):155–160, November 1998. doi: 10.1086/306333.

Romeel Davé, Mika H. Rafieferantsoa, Robert J. Thompson, and Philip F. Hopkins. MUFASA: Galaxy star formation, gas, and metal properties across cosmic time. *Monthly Notices of the Royal Astronomical Society*, 467(1):115–132, May 2017. doi: 10.1093/mnras/stx108.

Pratika Dayal, Marta Volonteri, Tirthankar Roy Choudhury, Raffaella Schneider, Maxime Trebitsch, Nickolay Y. Gnedin, Hakim Atek, Michaela Hirschmann, and Amy Reines. Reionization with galaxies and active galactic nuclei. *Monthly Notices of the Royal Astronomical Society*, 495(3):3065–3078, July 2020. doi: 10.1093/mnras/staa1138.

Claire Mackay Dickey, Marla Geha, Andrew Wetzel, and Kareem El-Badry. AGN All the Way Down? AGN-like Line Ratios Are Common in the Lowest-mass Isolated Quiescent Galaxies. *The Astrophysical Journal*, 884(2):180, October 2019. doi: 10.3847/1538-4357/ab3220.

V. M. Douna, L. J. Pellizza, I. F. Mirabel, and S. E. Pedrosa. Metallicity dependence of high-mass X-ray binary populations. *Astronomy & Astrophysics*, 579: A44, July 2015. doi: 10.1051/0004-6361/201525617.

Vanesa M. Douna, Leonardo J. Pellizza, Philippe Laurent, and I. Félix Mirabel. Microquasars as heating sources of the intergalactic medium during reionization of the Universe. *Monthly Notices of the Royal Astronomical Society*, 474(3): 3488–3499, March 2018. doi: 10.1093/mnras/stx2983.

P. A. Duc and I. F. Mirabel. Recycled galaxies in the colliding system ARP 105. *Astronomy & Astrophysics*, 289:83–93, September 1994.

R. S. Ellis. *Observations of the High Redshift Universe*, pages 259–364. 2008. doi: 10.1007/978-3-540-74163-3_3.

Sara L. Ellison, David R. Patton, Luc Simard, and Alan W. McConnachie. Clues to the Origin of the Mass-Metallicity Relation: Dependence on Star Formation Rate and Galaxy Size. *The Astrophysical Journal Letters*, 672(2):L107, January 2008. doi: 10.1086/527296.

Steven L. Finkelstein, Anson D'Aloisio, Jan-Pieter Paardekooper, Jr. Ryan, Russell, Peter Behroozi, Kristian Finlator, Rachael Livermore, Phoebe R. Upton Sanderbeck, Claudio Dalla Vecchia, and Sadegh Khochfar. Conditions for Reionizing the Universe with a Low Galaxy Ionizing Photon Escape Fraction. *The Astrophysical Journal*, 879(1):36, July 2019. doi: 10.3847/1538-4357/ab1ea8.

Francesca M. Fornasini, Francesca Civano, and Hyewon Suh. Connecting the metallicity dependence and redshift evolution of high-mass X-ray binaries. *Monthly Notices of the Royal Astronomical Society*, 495(1):771–783, June 2020. doi: 10.1093/mnras/staa1211.

T. Fragos, B. Lehmer, M. Tremmel, P. Tzanavaris, A. Basu-Zych, K. Belczynski, A. Hornschemeier, L. Jenkins, V. Kalogera, A. Ptak, and A. Zezas. X-Ray Binary Evolution Across Cosmic Time. *The Astrophysical Journal*, 764(1):41, February 2013. doi: 10.1088/0004-637X/764/1/41.

Michael J. Fromerth, Inga Kuznetsova, Lance Labun, Jean Letessier, and Jan Rafelski. From Quark-Gluon Universe to Neutrino Decoupling: 200¡T¡2MeV. *arXiv e-prints*, art. arXiv:1211.4297, November 2012.

Steven R. Furlanetto, Matias Zaldarriaga, and Lars Hernquist. The Growth of H II Regions During Reionization. *The Astrophysical Journal*, 613(1):1–15, September 2004. doi: 10.1086/423025.

D. R. Garnett and G. A. Shields. The Composition Gradient across M81. *The Astrophysical Journal*, 317:82, June 1987. doi: 10.1086/165257.

A. Georgakakis, J. Aird, A. Schulze, T. Dwelly, M. Salvato, K. Nandra, A. Merloni, and D. P. Schneider. Observational constraints on the specific accretion-rate distribution of X-ray-selected AGNs. *Monthly Notices of the Royal Astronomical Society*, 471(2):1976–2001, October 2017. doi: 10.1093/mnras/stx1602.

M. Gilfanov, H. J. Grimm, and R. Sunyaev. Statistical properties of the combined emission of a population of discrete sources: astrophysical implications. *Monthly Notices of the Royal Astronomical Society*, 351(4):1365–1378, July 2004. doi: 10.1111/j.1365-2966.2004.07874.x.

A. Grazian, E. Giallongo, K. Boutsia, S. Cristiani, E. Vanzella, C. Scarlata, P. Santini, L. Pentericci, E. Merlin, N. Menci, F. Fontanot, A. Fontana, F. Fiore, F. Civano, M. Castellano, M. Brusa, A. Bonchi, R. Carini, F. Cusano, M. Faccini, B. Garilli, A. Marchetti, A. Rossi, and R. Speziali. The contribution of faint AGNs to the ionizing background at z 4. *Astronomy & Astrophysics*, 613:A44, May 2018. doi: 10.1051/0004-6361/201732385.

James E. Gunn, Walter A. Siegmund, Edward J. Mannery, Russell E. Owen, Charles L. Hull, R. French Leger, Larry N. Carey, Gillian R. Knapp, Donald G. York, William N. Boroski, Stephen M. Kent, Robert H. Lupton, Constance M. Rockosi, Michael L. Evans, Patrick Waddell, John E. Anderson, James Annis, John C. Barentine, Larry M. Bartoszek, Steven Bastian, Stephen B. Bracker, Howard J. Brewington, Charles I. Briegel, Jon Brinkmann, Yorke J. Brown, Michael A. Carr, Paul C. Czarapata, Craig C. Drennan, Thomas Dombeck, Glenn R. Federwitz, Bruce A. Gillespie, Carlos Gonzales, Sten U. Hansen, Michael Harvanek, Jeffrey Hayes, Wendell Jordan, Ellyne Kinney, Mark Klaene, S. J. Kleinman, Richard G. Kron, Jurek Kresinski, Glenn Lee, Siriluk Limmongkol, Carl W. Lindenmeyer, Daniel C. Long, Craig L. Loomis, Peregrine M. McGehee, Paul M. Mantsch, Jr. Neilsen, Eric H., Richard M. Neswold, Peter R. Newman, Atsuko Nitta, Jr. Peoples, John, Jeffrey R. Pier, Peter S. Prieto, Angela Prosapio, Claudio Rivetta, Donald P. Schneider, Stephanie Snedden, and Shu-i. Wang. The 2.5 m Telescope of the

Sloan Digital Sky Survey. *The Astronomical Journal*, 131(4):2332–2359, April 2006. doi: 10.1086/500975.

N. G. Guseva, P. Papaderos, H. T. Meyer, Y. I. Izotov, and K. J. Fricke. An investigation of the luminosity-metallicity relation for a large sample of low-metallicity emission-line galaxies. *Astronomy & Astrophysics*, 505(1):63–72, October 2009. doi: 10.1051/0004-6361/200912414.

Natalia G. Guseva, Yuri I. Izotov, and Trinh X. Thuan. A Spectroscopic Study of a Large Sample Of Wolf-Rayet Galaxies. *The Astrophysical Journal*, 531(2): 776–803, March 2000. doi: 10.1086/308489.

Rafael Guzmán, Jesús Gallego, David C. Koo, Andrew C. Phillips, James D. Lowenthal, S. M. Faber, Garth D. Illingworth, and Nicole P. Vogt. The Nature of Compact Galaxies in the Hubble Deep Field. II. Spectroscopic Properties and Implications for the Evolution of the Star Formation Rate Density of the Universe1,. *The Astrophysical Journal*, 489(2):559–572, November 1997. doi: 10.1086/304797.

Kevin N. Hainline, Amy E. Reines, Jenny E. Greene, and Daniel Stern. Mid-infrared Colors of Dwarf Galaxies: Young Starbursts Mimicking Active Galactic Nuclei. *The Astrophysical Journal*, 832(2):119, December 2016. doi: 10.3847/0004-637X/832/2/119.

Timothy M. Heckman, Matthew D. Lehnert, David K. Strickland, and Lee Armus. Absorption-Line Probes of Gas and Dust in Galactic Superwinds. *The Astrophysical Journal Supplement*, 129(2):493–516, August 2000. doi: 10.1086/313421.

Alaina Henry, Claudia Scarlata, Crystal L. Martin, and Dawn Erb. Lyα Emission from Green Peas: The Role of Circumgalactic Gas Density, Covering, and Kinematics. *The Astrophysical Journal*, 809(1):19, August 2015. doi: 10.1088/0004-637X/809/1/19.

F. Hoyle and W. A. Fowler. On the nature of strong radio sources. *Monthly Notices of the Royal Astronomical Society*, 125:169, January 1963. doi: 10.1093/mnras/125.2.169.

Y. I. Izotov, T. X. Thuan, N. G. Guseva, and S. E. Liss. J0811+4730: the most metal-poor star-forming dwarf galaxy known. *Monthly Notices of the Royal*

Astronomical Society, 473(2):1956–1966, January 2018. doi: 10.1093/mnras/stx2478.

Yuri I. Izotov, Frederic H. Chaffee, Craig B. Foltz, Richard F. Green, Natalia G. Guseva, and Trinh X. Thuan. Helium Abundance in the Most Metal-deficient Blue Compact Galaxies: I ZW 18 and SBS 0335-052. *The Astrophysical Journal*, 527(2):757–777, December 1999. doi: 10.1086/308119.

Myoungwon Jeon, Andreas H. Pawlik, Volker Bromm, and Miloš Milosavljević. Radiative feedback from high-mass X-ray binaries on the formation of the first galaxies and early reionization. *Monthly Notices of the Royal Astronomical Society*, 440(4):3778–3796, June 2014. doi: 10.1093/mnras/stu444.

Stephen Justham and Kevin Schawinski. Another thread in the tapestry of stellar feedback: X-ray binaries. *Monthly Notices of the Royal Astronomical Society*, 423(2):1641–1651, June 2012. doi: 10.1111/j.1365-2966.2012.20985.x.

Philip Kaaret, Hua Feng, and Timothy P. Roberts. Ultraluminous X-Ray Sources. *Annual Review of Astronomy and Astrophysics*, 55(1):303–341, August 2017. doi: 10.1146/annurev-astro-091916-055259.

Koki Kakiichi, Richard S. Ellis, Nicolas Laporte, Adi Zitrin, Anna-Christina Eilers, Emma Ryan-Weber, Romain A. Meyer, Brant Robertson, Daniel P. Stark, and Sarah E. I. Bosman. The role of galaxies and AGN in reionizing the IGM - I. Keck spectroscopy of 5 ¡ z ¡ 7 galaxies in the QSO field J1148+5251. *Monthly Notices of the Royal Astronomical Society*, 479(1):43–63, September 2018. doi: 10.1093/mnras/sty1318.

Igor D. Karachentsev, Valentina E. Karachentseva, Walter K. Huchtmeier, and Dmitry I. Makarov. A Catalog of Neighboring Galaxies. *The Astronomical Journal*, 127(4):2031–2068, April 2004. doi: 10.1086/382905.

Guinevere Kauffmann, Timothy M. Heckman, Christy Tremonti, Jarle Brinchmann, Stéphane Charlot, Simon D. M. White, Susan E. Ridgway, Jon Brinkmann, Masataka Fukugita, Patrick B. Hall, Željko Ivezić, Gordon T. Richards, and Donald P. Schneider. The host galaxies of active galactic nuclei. *Monthly Notices of the Royal Astronomical Society*, 346(4):1055–1077, December 2003a. doi: 10.1111/j.1365-2966.2003.07154.x.

Guinevere Kauffmann, Timothy M. Heckman, Simon D. M. White, Stéphane Charlot, Christy Tremonti, Jarle Brinchmann, Gustavo Bruzual, Eric W. Peng, Mark Seibert, Mariangela Bernardi, Michael Blanton, Jon Brinkmann, Francisco Castander, Istvan Csábai, Masataka Fukugita, Zeljko Ivezic, Jeffrey A. Munn, Robert C. Nichol, Nikhil Padmanabhan, Aniruddha R. Thakar, David H. Weinberg, and Donald York. Stellar masses and star formation histories for 10^5 galaxies from the Sloan Digital Sky Survey. *Monthly Notices of the Royal Astronomical Society*, 341(1):33–53, May 2003b. doi: 10.1046/j.1365-8711.2003.06291.x.

Guinevere Kauffmann, Timothy M. Heckman, Simon D. M. White, Stéphane Charlot, Christy Tremonti, Eric W. Peng, Mark Seibert, Jon Brinkmann, Robert C. Nichol, Mark SubbaRao, and Don York. The dependence of star formation history and internal structure on stellar mass for 10^5 low-redshift galaxies. *Monthly Notices of the Royal Astronomical Society*, 341(1):54–69, May 2003c. doi: 10.1046/j.1365-8711.2003.06292.x.

Jr. Kennicutt, Robert C. Star Formation in Galaxies Along the Hubble Sequence. *Annual Review of Astronomy and Astrophysics*, 36:189–232, January 1998. doi: 10.1146/annurev.astro.36.1.189.

Robert C. Kennicutt and Neal J. Evans. Star Formation in the Milky Way and Nearby Galaxies. *Annual Review of Astronomy and Astrophysics*, 50:531–608, September 2012. doi: 10.1146/annurev-astro-081811-125610.

L. J. Kewley, M. A. Dopita, R. S. Sutherland, C. A. Heisler, and J. Trevena. Theoretical Modeling of Starburst Galaxies. *The Astrophysical Journal*, 556 (1):121–140, July 2001. doi: 10.1086/321545.

Lisa J. Kewley, Michael A. Dopita, Claus Leitherer, Romeel Davé, Tiantian Yuan, Mark Allen, Brent Groves, and Ralph Sutherland. Theoretical Evolution of Optical Strong Lines across Cosmic Time. *The Astrophysical Journal*, 774(2): 100, September 2013. doi: 10.1088/0004-637X/774/2/100.

G. Knevitt, G. A. Wynn, C. Power, and J. S. Bolton. Heating and ionization of the primordial intergalactic medium by high-mass X-ray binaries. *Monthly Notices of the Royal Astronomical Society*, 445(2):2034–2048, December 2014. doi: 10.1093/mnras/stu1803.

Mikkel T. Kristensen, Kevin Pimbblet, and Samantha Penny. Environments of dwarf galaxies with optical AGN characteristics. *Monthly Notices of the Royal Astronomical Society*, 496(3):2577–2590, August 2020. doi: 10.1093/mnras/staa1719.

Mark R. Krumholz. Star Formation in Molecular Clouds. In Eduardo Telles, Renato Dupke, and Daniela Lazzaro, editors, *XV Special Courses at the National Observatory of Rio de Janeiro*, volume 1386 of *American Institute of Physics Conference Series*, pages 9–57, September 2011. doi: 10.1063/1.3636038.

D. Kunth and G. Östlin. The most metal-poor galaxies. *Astronomy & Astrophysicsr*, 10:1–79, January 2000. doi: 10.1007/s001590000005.

Daniel Kunth, J. M. Mas-Hesse, E. Terlevich, R. Terlevich, J. Lequeux, and S. Michael Fall. HST study of Lyman-alpha emission in star-forming galaxies: the effect of neutral gas flows. *Astronomy & Astrophysics*, 334:11–20, June 1998.

Janice C. Lee, Jr. Kennicutt, Robert C., S. J. José G. Funes, Shoko Sakai, and Sanae Akiyama. Dwarf Galaxy Starburst Statistics in the Local Volume. *The Astrophysical Journal*, 692(2):1305–1320, February 2009. doi: 10.1088/0004-637X/692/2/1305.

B. D. Lehmer, D. M. Alexander, F. E. Bauer, W. N. Brandt, A. D. Goulding, L. P. Jenkins, A. Ptak, and T. P. Roberts. A Chandra Perspective on Galaxy-wide X-ray Binary Emission and its Correlation with Star Formation Rate and Stellar Mass: New Results from Luminous Infrared Galaxies. *The Astrophysical Journal*, 724(1):559–571, November 2010. doi: 10.1088/0004-637X/724/1/559.

B. D. Lehmer, A. R. Basu-Zych, S. Mineo, W. N. Brandt, R. T. Eufrasio, T. Fragos, A. E. Hornschemeier, B. Luo, Y. Q. Xue, F. E. Bauer, M. Gilfanov, P. Ranalli, D. P. Schneider, O. Shemmer, P. Tozzi, J. R. Trump, C. Vignali, J. X. Wang, M. Yukita, and A. Zezas. The Evolution of Normal Galaxy X-Ray Emission through Cosmic History: Constraints from the 6 MS Chandra Deep Field-South. *The Astrophysical Journal*, 825(1):7, July 2016. doi: 10.3847/0004-637X/825/1/7.

Bret D. Lehmer, Rafael T. Eufrasio, Antara Basu-Zych, Keith Doore, Tassos Fragos, Kristen Garofali, Konstantinos Kovlakas, Benjamin F. Williams, Andreas

Zezas, and Luidhy Santana-Silva. The Metallicity Dependence of the High-mass X-Ray Binary Luminosity Function. *The Astrophysical Journal*, 907(1): 17, January 2021. doi: 10.3847/1538-4357/abcec1.

Claus Leitherer, Rupali Chandar, Christy A. Tremonti, Aida Wofford, and Daniel Schaerer. Far-ultraviolet Observations of Outflows from Infrared-luminous Galaxies. *The Astrophysical Journal*, 772(2):120, August 2013. doi: 10.1088/0004-637X/772/2/120.

J. Lequeux, M. Peimbert, J. F. Rayo, A. Serrano, and S. Torres-Peimbert. Reprint of 1979A&A....80..155L. Chemical composition and evolution of irregular and blue compact galaxies. *Astronomy & Astrophysics*, 500:145–156, December 1979.

Abraham Loeb. First Light. *arXiv e-prints*, art. astro-ph/0603360, March 2006.

G. Marconi, F. Matteucci, and M. Tosi. Element abundances in blue compact galaxies. *Monthly Notices of the Royal Astronomical Society*, 270:35–45, September 1994. doi: 10.1093/mnras/270.1.35.

Avery Meiksin and Piero Madau. On the Photoionization of the Intergalactic Medium by Quasars at High Redshift. *The Astrophysical Journal*, 412:34, July 1993. doi: 10.1086/172898.

Mar Mezcua and Helena Domínguez Sánchez. Hidden AGNs in Dwarf Galaxies Revealed by MaNGA: Light Echoes, Off-nuclear Wanderers, and a New Broad-line AGN. *The Astrophysical Journal Letters*, 898(2):L30, August 2020. doi: 10.3847/2041-8213/aba199.

S. Mineo, M. Gilfanov, and R. Sunyaev. X-ray emission from star-forming galaxies - I. High-mass X-ray binaries. *Monthly Notices of the Royal Astronomical Society*, 419(3):2095–2115, January 2012a. doi: 10.1111/j.1365-2966.2011.19862.x.

S. Mineo, M. Gilfanov, and R. Sunyaev. X-ray emission from star-forming galaxies - II. Hot interstellarmedium. *Monthly Notices of the Royal Astronomical Society*, 426(3):1870–1883, November 2012b. doi: 10.1111/j.1365-2966.2012.21831.x.

S. Mineo, M. Gilfanov, B. D. Lehmer, G. E. Morrison, and R. Sunyaev. X-ray emission from star-forming galaxies - III. Calibration of the L_X-SFR relation

up to redshift z ≈ 1.3. *Monthly Notices of the Royal Astronomical Society*, 437 (2):1698–1707, January 2014. doi: 10.1093/mnras/stt1999.

S. Mitra, T. R. Choudhury, and A. Ferrara. Cosmic reionization after Planck. *Monthly Notices of the Royal Astronomical Society*, 454:L76–L80, November 2015. doi: 10.1093/mnrasl/slv134.

Sourav Mitra, T. Roy Choudhury, and Andrea Ferrara. Cosmic reionization after Planck II: contribution from quasars. *Monthly Notices of the Royal Astronomical Society*, 473(1):1416–1425, January 2018. doi: 10.1093/mnras/stx2443.

Edward C. Moran, Alexei V. Filippenko, and Ryan Chornock. "Hidden" Seyfert 2 Galaxies and the X-Ray Background. *The Astrophysical Journal Letters*, 579 (2):L71–L74, November 2002. doi: 10.1086/345314.

K. Nandra and K. A. Pounds. GINGA observations of the X-ray spectra of Seyfert galaxies. *Monthly Notices of the Royal Astronomical Society*, 268:405–429, May 1994. doi: 10.1093/mnras/268.2.405.

Masafusa Onoue, Nobunari Kashikawa, Chris J. Willott, Pascale Hibon, Myung-shin Im, Hisanori Furusawa, Yuichi Harikane, Masatoshi Imanishi, Shogo Ishikawa, Satoshi Kikuta, Yoshiki Matsuoka, Tohru Nagao, Yuu Niino, Yoshi-aki Ono, Masami Ouchi, Masayuki Tanaka, Ji-Jia Tang, Jun Toshikawa, and Hisakazu Uchiyama. Minor Contribution of Quasars to Ionizing Photon Budget at z ∼ 6: Update on Quasar Luminosity Function at the Faint End with Subaru/Suprime-Cam. *The Astrophysical Journal Letters*, 847(2):L15, October 2017. doi: 10.3847/2041-8213/aa8cc6.

I. Orlitová, A. Verhamme, A. Henry, C. Scarlata, A. Jaskot, M. S. Oey, and D. Schaerer. Puzzling Lyman-alpha line profiles in green pea galaxies. *Astronomy & Astrophysics*, 616:A60, August 2018. doi: 10.1051/0004-6361/201732478.

Ivana Orlitová. Starburst galaxies. *arXiv e-prints*, art. arXiv:2012.12378, December 2020.

Shaghayegh Parsa, James S. Dunlop, and Ross J. McLure. No evidence for a significant AGN contribution to cosmic hydrogen reionization. *Monthly Notices of the Royal Astronomical Society*, 474(3):2904–2923, March 2018. doi: 10.1093/mnras/stx2887.

Max Pettini and Bernard E. J. Pagel. [OIII]/[NII] as an abundance indicator at high redshift. *Monthly Notices of the Royal Astronomical Society*, 348(3): L59–L63, March 2004. doi: 10.1111/j.1365-2966.2004.07591.x.

E. Piconcelli, E. Jimenez-Bailón, M. Guainazzi, N. Schartel, P. M. Rodríguez-Pascual, and M. Santos-Lleó. The XMM-Newton view of PG quasars. I. X-ray continuum and absorption. *Astronomy & Astrophysics*, 432(1):15–30, March 2005. doi: 10.1051/0004-6361:20041621.

L. S. Pilyugin and L. Mattsson. Abundance determination in H II regions from spectra without the [O II]λ3727+λ3729 line. *Monthly Notices of the Royal Astronomical Society*, 412(2):1145–1150, April 2011. doi: 10.1111/j.1365-2966. 2010.17970.x.

Planck Collaboration, N. Aghanim, Y. Akrami, M. Ashdown, J. Aumont, C. Baccigalupi, M. Ballardini, A. J. Banday, R. B. Barreiro, N. Bartolo, S. Basak, R. Battye, K. Benabed, J. P. Bernard, M. Bersanelli, P. Bielewicz, J. J. Bock, J. R. Bond, J. Borrill, F. R. Bouchet, F. Boulanger, M. Bucher, C. Burigana, R. C. Butler, E. Calabrese, J. F. Cardoso, J. Carron, A. Challinor, H. C. Chiang, J. Chluba, L. P. L. Colombo, C. Combet, D. Contreras, B. P. Crill, F. Cuttaia, P. de Bernardis, G. de Zotti, J. Delabrouille, J. M. Delouis, E. Di Valentino, J. M. Diego, O. Doré, M. Douspis, A. Ducout, X. Dupac, S. Dusini, G. Efstathiou, F. Elsner, T. A. Enßlin, H. K. Eriksen, Y. Fantaye, M. Farhang, J. Fergusson, R. Fernandez-Cobos, F. Finelli, F. Forastieri, M. Frailis, A. A. Fraisse, E. Franceschi, A. Frolov, S. Galeotta, S. Galli, K. Ganga, R. T. Génova-Santos, M. Gerbino, T. Ghosh, J. González-Nuevo, K. M. Górski, S. Gratton, A. Gruppuso, J. E. Gudmundsson, J. Hamann, W. Handley, F. K. Hansen, D. Herranz, S. R. Hildebrandt, E. Hivon, Z. Huang, A. H. Jaffe, W. C. Jones, A. Karakci, E. Keihänen, R. Keskitalo, K. Kiiveri, J. Kim, T. S. Kisner, L. Knox, N. Krachmalnicoff, M. Kunz, H. Kurki-Suonio, G. Lagache, J. M. Lamarre, A. Lasenby, M. Lattanzi, C. R. Lawrence, M. Le Jeune, P. Lemos, J. Lesgourgues, F. Levrier, A. Lewis, M. Liguori, P. B. Lilje, M. Lilley, V. Lindholm, M. López-Caniego, P. M. Lubin, Y. Z. Ma, J. F. Macías-Pérez, G. Maggio, D. Maino, N. Mandolesi, A. Mangilli, A. Marcos-Caballero, M. Maris, P. G. Martin, M. Martinelli, E. Martínez-González, S. Matarrese, N. Mauri, J. D. McEwen, P. R. Meinhold, A. Melchiorri, A. Mennella, M. Migliaccio, M. Millea, S. Mitra, M. A. Miville-Deschênes, D. Molinari, L. Montier, G. Mor-

gante, A. Moss, P. Natoli, H. U. Nørgaard-Nielsen, L. Pagano, D. Paoletti, B. Partridge, G. Patanchon, H. V. Peiris, F. Perrotta, V. Pettorino, F. Piacentini, L. Polastri, G. Polenta, J. L. Puget, J. P. Rachen, M. Reinecke, M. Remazeilles, A. Renzi, G. Rocha, C. Rosset, G. Roudier, J. A. Rubiño-Martín, B. Ruiz-Granados, L. Salvati, M. Sandri, M. Savelainen, D. Scott, E. P. S. Shellard, C. Sirignano, G. Sirri, L. D. Spencer, R. Sunyaev, A. S. Suur-Uski, J. A. Tauber, D. Tavagnacco, M. Tenti, L. Toffolatti, M. Tomasi, T. Trombetti, L. Valenziano, J. Valiviita, B. Van Tent, L. Vibert, P. Vielva, F. Villa, N. Vittorio, B. D. Wandelt, I. K. Wehus, M. White, S. D. M. White, A. Zacchei, and A. Zonca. Planck 2018 results. VI. Cosmological parameters. *Astronomy & Astrophysics*, 641:A6, September 2020. doi: 10.1051/0004-6361/201833910.

P. Ranalli, A. Comastri, and G. Setti. The 2-10 keV luminosity as a Star Formation Rate indicator. *Astronomy & Astrophysics*, 399:39–50, February 2003. doi: 10.1051/0004-6361:20021600.

Brant E. Robertson, Richard S. Ellis, James S. Dunlop, Ross J. McLure, and Daniel P. Stark. Early star-forming galaxies and the reionization of the Universe. *Nature*, 468(7320):49–55, November 2010. doi: 10.1038/nature09527.

S. R. Rosen, N. A. Webb, M. G. Watson, J. Ballet, D. Barret, V. Braito, F. J. Carrera, M. T. Ceballos, M. Coriat, R. Della Ceca, G. Denkinson, P. Esquej, S. A. Farrell, M. Freyberg, F. Grisé, P. Guillout, L. Heil, F. Koliopanos, D. Law-Green, G. Lamer, D. Lin, R. Martino, L. Michel, C. Motch, A. Nebot Gomez-Moran, C. G. Page, K. Page, M. Page, M. W. Pakull, J. Pye, A. Read, P. Rodriguez, M. Sakano, R. Saxton, A. Schwope, A. E. Scott, R. Sturm, I. Traulsen, V. Yershov, and I. Zolotukhin. The XMM-Newton serendipitous survey. VII. The third XMM-Newton serendipitous source catalogue. *Astronomy & Astrophysics*, 590:A1, May 2016. doi: 10.1051/0004-6361/201526416.

E. E. Salpeter. Accretion of Interstellar Matter by Massive Objects. *The Astrophysical Journal*, 140:796–800, August 1964. doi: 10.1086/147973.

M. Schmidt. 3C 273 : A Star-Like Object with Large Red-Shift. *Nature*, 197 (4872):1040, March 1963. doi: 10.1038/1971040a0.

Peter Schneider. *Extragalactic Astronomy and Cosmology: An Introduction*. 2015. doi: 10.1007/978-3-642-54083-7.

Norbert S. Schulz. *From Dust To Stars Studies of the Formation and Early Evolution of Stars.* 2005. doi: 10.1007/b138917.

Yue Shen, Gordon T. Richards, Michael A. Strauss, Patrick B. Hall, Donald P. Schneider, Stephanie Snedden, Dmitry Bizyaev, Howard Brewington, Viktor Malanushenko, Elena Malanushenko, Dan Oravetz, Kaike Pan, and Audrey Simmons. A Catalog of Quasar Properties from Sloan Digital Sky Survey Data Release 7. *The Astrophysical Journal Supplement*, 194(2):45, June 2011. doi: 10.1088/0067-0049/194/2/45.

Evan D. Skillman, R. C. Kennicutt, and P. W. Hodge. Oxygen Abundances in Nearby Dwarf Irregular Galaxies. *The Astrophysical Journal*, 347:875, December 1989. doi: 10.1086/168178.

J. Svoboda, M. Guainazzi, and A. Merloni. AGN spectral states from simultaneous UV and X-ray observations by XMM-Newton. *Astronomy & Astrophysics*, 603:A127, July 2017. doi: 10.1051/0004-6361/201630181.

J. Svoboda, V. Douna, I. Orlitová, and M. Ehle. Green Peas in X-Rays. *The Astrophysical Journal*, 880(2):144, August 2019. doi: 10.3847/1538-4357/ab2b39.

Núria Torres-Albà, Valentí Bosch-Ramon, and Kazushi Iwasawa. AGN jets versus accretion as reionization sources. *Astronomy & Astrophysics*, 635:A57, March 2020. doi: 10.1051/0004-6361/201936047.

Christy A. Tremonti, Timothy M. Heckman, Guinevere Kauffmann, Jarle Brinchmann, Stéphane Charlot, Simon D. M. White, Mark Seibert, Eric W. Peng, David J. Schlegel, Alan Uomoto, Masataka Fukugita, and Jon Brinkmann. The Origin of the Mass-Metallicity Relation: Insights from 53,000 Star-forming Galaxies in the Sloan Digital Sky Survey. *The Astrophysical Journal*, 613(2):898–913, October 2004. doi: 10.1086/423264.

Jonathan R. Trump, Mouyuan Sun, Gregory R. Zeimann, Cuyler Luck, Joanna S. Bridge, Catherine J. Grier, Alex Hagen, Stephanie Juneau, Antonio Montero-Dorta, David J. Rosario, W. Niel Brandt, Robin Ciardullo, and Donald P. Schneider. The Biases of Optical Line-Ratio Selection for Active Galactic Nuclei and the Intrinsic Relationship between Black Hole Accretion and Galaxy Star Formation. *The Astrophysical Journal*, 811(1):26, September 2015. doi: 10.1088/0004-637X/811/1/26.

M. Tueros, M. V. del Valle, and G. E. Romero. Cosmic reionization by primordial cosmic rays. *Astronomy & Astrophysics*, 570:L3, October 2014. doi: 10.1051/0004-6361/201424666.

Derek Ward-Thompson and Anthony P. Whitworth. *An Introduction to Star Formation.* 2011.

John H. Wise. Cosmic reionisation. *Contemporary Physics*, 60(2):145–163, April 2019. doi: 10.1080/00107514.2019.1631548.

Saleem Zaroubi. *The Epoch of Reionization*, volume 396, page 45. 2013. doi: 10.1007/978-3-642-32362-1aap_2.

Dong Zhang. A Review of the Theory of Galactic Winds Driven by Stellar Feedback. *Galaxies*, 6(4):114, November 2018. doi: 10.3390/galaxies6040114.

List of Figures

List of Tables

List of Abbreviations

AGN - Active Galactic Nucleus

BCG - Blue Compact Galaxy

ESA - European Space Agency

GP - Green Pea

HMXB - High-mass X-ray binary

IGM - Intergalactic medium

IMBH - Intermediate-mass black hole

IR - Infrared

ISM - Interstellar medium

LAE - Lyman-Alpha Emitter

LBA - Lyman-break analogue

LIRG - Luminous infrared galaxy

LMXB - Low-mass X-ray binary

QSO - Quasi-stellar object

SDSS - Sloan Digital Sky Survey

SFDG - Star-forming dwarf galaxy

SFG - Star-forming galaxy

SFR - Star formation rate

SMBH - Supermassive black hole

sSFR - Specific star formation rate

ULX - Ultra-luminous X-ray source

UV - Ultraviolet

XMM-Newton - X-ray Multi-Mirror Mission

XRB - X-ray binary